Three-Dimensional Thermo-Elasto-Hydrodynamic Computational Fluid Dynamics Model of a Tilting Pad Journal Bearing—Part I: Static Response

Jongin Yang
Mem. ASME
Department of Mechanical Engineering,
Texas A&M University,
College Station, TX 77840
e-mail: jiyang@tamu.edu

Alan Palazzolo
James J. Cain Professor I
Fellow ASME
Department of Mechanical Engineering,
Texas A&M University,
College Station, TX 77840
e-mail: a-palazzolo@tamu.edu

This paper presents the first simulation model of a tilting pad journal bearing (TPJB) using three-dimensional (3D) computational fluid dynamics (CFD), including multiphase flow, thermal-fluid, transitional turbulence, and thermal deformation of the shaft and pads employing two-way fluid–structure interaction (FSI). Part I presents a modeling method for the static performance. The model includes flow between pads BP, which eliminates the use of an uncertain, mixing coefficient (MC) in Reynold's equation approaches. The CFD model is benchmarked with Reynold's model with a 3D thermal-film, when the CFD model boundary conditions are consistent with the Reynolds boundary conditions. The Reynolds model employs an oversimplified MC representation of the three-dimensional mixing effect of the BP flow and heat transfer, and it also employs simplifying assumptions for the flow and heat transfer within the thin film between the journal and bearing. This manufactured comparison shows good agreement between the CFD and Reynold's equation models. The CFD model is generalized by removing these fictitious boundary conditions on pad inlets and outlets and instead models the flow and temperature between pads. The results show that Reynold's model MC approach can lead to significant differences with the CFD model including detailed flow and thermal modeling between pads. Thus, the CFD approach provides increased reliability of predictions. The paper provides an instructive methodology including detailed steps for properly applying CFD to tilt pad bearing modeling. Parts I and II focus on predicting static and dynamic response characteristic responses, respectively. [DOI: 10.1115/1.4043349]

1 Introduction

Tilting pad journal bearing (TPJB) performance predictions have been obtained via Reynolds equation solvers and with computational fluid dynamics (CFD) codes. Most of the research for TPJB performance has utilized the Reynolds model. In 1973, Tieu [1] applied the finite element method to solve the energy equation with the variable viscosity for infinitely wide bearings. In 1980, Ettles [2] combined the one-dimensional (1D) Reynolds and energy equations with a beam model for elastic—thermal—hydrodynamic modeling of TPJBs. In 1988, Knight and Barrett [3] utilized simplified Reynolds and 1D energy equations to model TPJBs, without shaft and pad distortions. In 1989, Brugier and Pascal [4] took into consideration the generalized Reynolds equation, 3D energy equation, pivot flexibility, and thermal and elastic deformation of the pads, assuming that the shaft temperature was constant. In 1990, Taniguchi et al. [5] performed TPJB three-dimensional (3D) thermo-hydrodynamic (THD) modeling with linearized turbulent lubrication theory and with neglect of pad and shaft distortions. In 1994, Kim et al. [6] presented a TPJB model including a generalized Reynolds equation, two-dimensional (2D) energy equation for the fluid-film and each pad, pivot flexibility, and shaft and pad distortions. In 2010, Haugaard and Santos [7] investigated the performance of a TPJB with controllable oil injection and employed modal reduction to reduce computations. In 2015, Suh and Palazzolo [8] presented a high-fidelity TPJB model using modal reduction, the generalized Reynolds equation, the 3D energy equation for the fluid-film, flexible pads, and shaft and pivot flexibility. The developed thermo-elasto-hydrodynamic (TEHD) modeling was also utilized to predict the Morton phenomena in TPJB [9]. In 2016, Dang et al. [10] investigated the effect of the load direction on nonnominal TPJB. The researchers showed the significance of the load direction and nonnominal geometry on the TPJB performance. In their subsequent research [11], they conducted a numerical study to predict the TPJB performance with manufacturing uncertainty. The numerical simulation was performed based on the Reynolds equation approach with a 2D energy equation.

An important consideration in the Reynolds TPJB THD modeling is the determination of the oil film inlet temperature at the leading edge of each pad [5]. In 1967, Ettles [12] introduced the hot oil carry over factor for the oil inlet groove of a thrust bearing obtained with 2D Navier–Stokes (NS) and energy equation solutions. In 1969, Ettles [13] showed the existence of the hot oil carry over effect from published experimental results for the various types of thrust bearings. In 1983, Mitsui et al. [14] proposed a modified form of the hot oil carry over factor from heat balance, with a mixing coefficient (MC) for the oil inlet groove of a circular journal bearing. It was experimentally estimated that MC ranged from 0.4 to 1.0. In 1986, Heshmat and Pinkus [15] presented empirical equations for MC of both journal and thrust bearings, as a function of operating conditions and bearing sizes. In 1986, Boncompain et al. [16] applied the assumptions that the inlet temperature of the oil film varies parabolically across the film thickness, and energy is conserved in the mixing area for TEHD analysis of a journal bearing.

Most researchers [2–6,9–11] have applied mixing theory based on heat balance in the mixing region for the performance prediction of a TPJB. Suh and Palazzolo [8] presented a modified mixing theory. They introduced an approach to treat all cases of relative flows between pad outlet flows and pad inlet flows. Although this

Contributed by the Tribology Division of ASME for publication in the JOURNAL OF TRIBOLOGY. Manuscript received October 26, 2018; final manuscript received March 27, 2019; published online April 30, 2019. Assoc. Editor: Stephen Boedo.

enhanced the applicability of the mixing theory approach, it was still susceptible to errors caused by the uncertainty of the MCs.

Computational fluid dynamics modeling can eliminate the uncertainty with mixing theory in the Reynolds model. The use of CFD for TPJB modeling has become possible owing to the rapid development of computer technology [17]. The literature contains many references for the CFD modeling of the fixed pad, plain journal bearings. Chen and Hahn [18] applied CFD to hydrodynamic bearing modeling including slider bearings, step bearings, journal bearings, and squeeze film dampers. Guo et al. [19] predicted the static and dynamic performance of hydrodynamic, hydrostatic, and hybrid journal bearings. Their CFD model solved the full NS equation and energy equation of the fluid-film with the varying viscosity, and detailed geometry of the oil inlet groove was considered. Shenoy et al. [20] presented a fluid–structure interaction (FSI)-CFD modeling methodology without thermal effects for a journal bearing. Liu et al. [21] developed an FSI-CFD model of a rotor-bearing system and investigated the effect of the rotor and bearing elastic deformation and dynamic unbalanced load on journal bearing performance. Thermal effects and oil inlet groove modeling were not considered in their model. Lin et al. [17] conducted a transient analysis of an FSI-CFD model for a flexible rotor-bearing system including thermal effects and considering the geometry of several oil inlet grooves.

A relatively small number of papers have reported on TPJB modeling using CFD due to its highly complex geometry. Edney et al. [22] analyzed the 2D turbulent flow with CFD for a single pad of a TPJB with a leading edge groove. The k-ε turbulence model was employed without considering thermal effects and a transition turbulence model. The model consisted of a 2D slice through a single pad with its equilibrium state determined in a conventional manner. Armentrout et al. [23] developed a CFD model for a water-lubricated TPJB, including a k-ω turbulence model for a 3D single pad. Searching shaft-pad motions for the equilibrium state, thermal effects, and geometry of the oil inlet grooves were not considered. The results of the CFD model were compared with the Reynolds model.

The present work presents an FSI-CFD model of a complete TPJB with the oil inlet groove, including incompressible multiphase flow, thermal-fluid effects, transition turbulence, shaft-pad heat conduction, nonlinear pivot flexibility, and a shaft-pad motion search for equilibrium conditions. This model is used to investigate the reliability of the Reynolds model's MC approach compared with the full CFD model including flow between pads. A significant variation of results is shown to occur when varying the MC through typical ranges, when compared with the CFD model results. This emphasizes a need to carefully select MCs for accurate predictions with the Reynolds model approach, or to utilize the CFD approach, thereby eliminating the need for guessing an MC.

The original contributions of this paper include the following:

(a) The first TEHD modeling methodology for static performance prediction of a TPJB using CFD with detailed 3D BP modeling.
(b) Demonstration that the conventional Reynolds model results may have a considerable uncertainty due to the uncertainty of the assumed MC between pads.
(c) The conventional (Reynolds) model results can have significant differences for TPJB static performance prediction compared with the high-fidelity CFD model due to the neglect of the axial and radial distribution of temperatures at the pad inlet in the Reynolds model.
(d) Provides a significant advance in the understanding of the heat transfer in the shaft.

2 Description of Fluid Structure Interaction—Computational Fluid Dynamics Model

2.1 Overall Description. The lubricant oil is supplied to between pads BP and discharged to the side outlet via circulation and the mixing process between pads. The total model includes

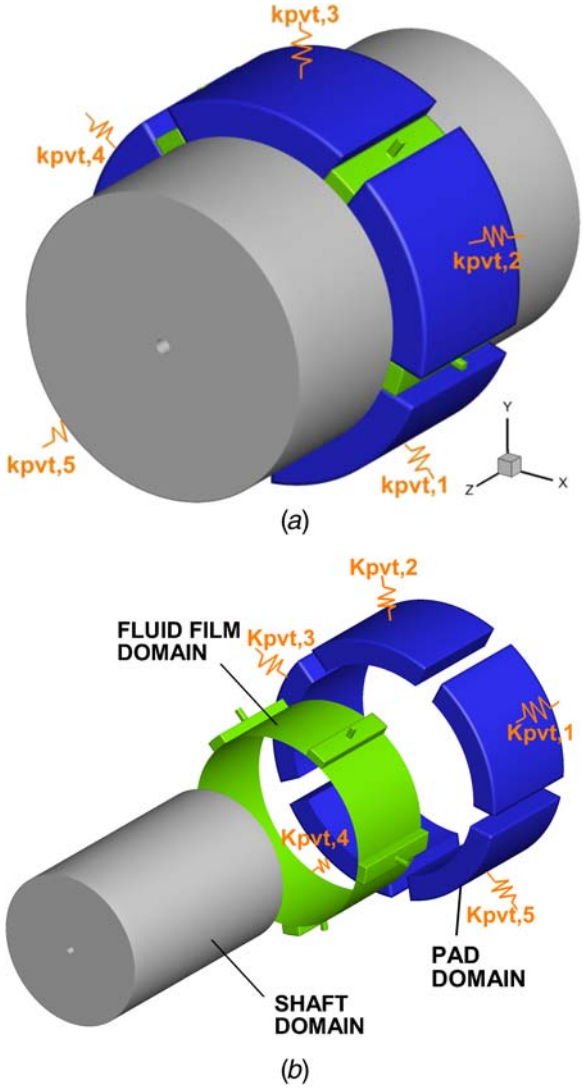

Fig. 1 Configuration of tilting pad journal bearing model: (*a*) assembled view and (*b*) exploded view

the shaft, pad, and fluid-film domains as represented in Fig. 1. The shaft and pad domains are elastic solids. The solid and fluid domains are connected by interface boundaries.

The fluid–structure interaction computational fluid dynamics (FSI-CFD) modeling approach includes meshing, geometry, CFD, and finite element analysis (FEA) solvers, which are included in the commercial code ANSYS. The computational components and their interactions are illustrated in Fig. 2. The geometry and mesh are shared by both CFD and FEA solvers. Each solver includes submodels to provide all required multiphysics features of the TPJB simulation. CFX is adopted as the CFD solver to solve the NS equation for the full fluid domain. Turbulence is known to occur in the BP fluid domain as initially indicated by Ettles [12], who emphasized the necessity of modeling the turbulence effect. The flow regime can be classified to be fully turbulent, partially turbulent with partially laminar, or fully laminar, according to operating speeds and geometry dimensions. The shear stress transport (SST) k-w turbulence model with transitional capability is employed for the flow regime. The fluid solver includes the solution of the energy equation with the temperature-dependent exponential varying viscosity, including viscous dissipation. In addition, the Rayleigh–Plesset cavitation model is utilized to model the phase change, which can occur below the saturation pressure. The CFD model has the advantage of dispensing with the need for an MC, which is necessary with the Reynolds approach, since the CFD

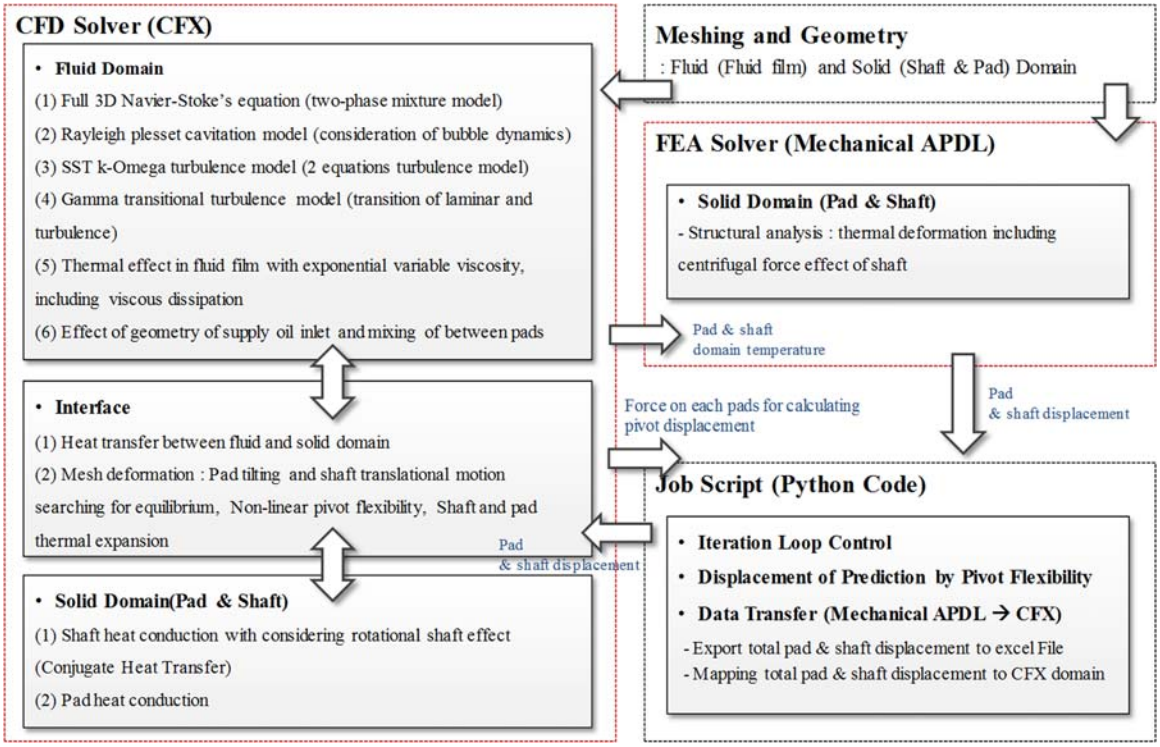

Fig. 2 Computation structure of the FSI-CFD TPJB model for the static response

model accounts for the effect of the geometry of the supply oil inlet and mixing without any assumptions. The solid domains of the CFD solver model heat conduction, and the rotational shaft effect is included in the energy equation with convective terms. The interface boundaries of the CFD solver take account of the shaft translational motions, pad tilting motions, pivot flexibility, and thermal deformation, in addition to the heat transfer between the fluid and solid domains. The interface boundaries are prescribed by mesh deformation functions, which are treated in Secs. 2.3 and 2.4. Detailed modeling techniques are provided in the following sections. In addition, the Mechanical APDL is chosen as the FEA solver to obtain structural deformations to predict displacements due to the thermal expansion and the centrifugal force.

The CFD and FEA solvers are coupled codewise with a job script function written in PYTHON. The job script iterates the solvers while transferring the results to each other. During the iterations, the temperature of the solid domains in the CFD solver is transferred to that in the FEA solver after completing predetermined iterations of the CFD solver. The FEA solver then calculates the displacement of the solid domains, and the results are transferred to the interface boundaries of the CFD solver. In addition, job script calculates the pivot displacement from the force on the pads that are obtained in the CFD sover, and it is transferred to the CFD solver. All these procedures are controlled by the job script, and the calculation continues until all residuals satisfy the convergence criteria.

2.2 Governing Equation of Computational Fluid Dynamics Solver. The Reynolds-averaged Navier–Stokes (RANS) equation is employed to model turbulence, which is derived from a statistical averaging procedure. The incompressible Reynolds-averaged continuity, momentum, and energy equations are given below in order.

$$\frac{\partial \rho_f}{\partial t} + \frac{\partial}{\partial x_i}(\rho_f u_i) = 0 \tag{1}$$

$$\frac{\partial \rho_f u_i}{\partial t} + \frac{\partial}{\partial x_j}(\rho_f u_i u_j) = -\frac{\partial p'}{\partial x_i} + \frac{\partial}{\partial x_j}\left[\mu_{eff}\left(\frac{\partial u_i}{\partial x_j} + \frac{\partial u_j}{\partial x_i}\right)\right] + S_M \tag{2}$$

$$\frac{\partial \rho_f h_{tot}}{\partial t} - \frac{\partial p}{\partial t} + \frac{\partial}{\partial x_j}(\rho_f u_j h_{tot}) = \frac{\partial}{\partial x_j}\left(\lambda_f \frac{\partial T_f}{\partial x_j} + \frac{\mu_t}{\mathrm{Pr}_t}\frac{\partial h_f}{\partial x_j}\right) + \frac{\partial}{\partial x_j}[u_i(\tau_{ij} - \rho_f \overline{u_i u_j})] + S_E \tag{3}$$

The thermal-fluid effect in the fluid-film of a TPJB is important because the dynamic viscosity is an exponential function of temperature and may vary significantly when operating under high-speed conditions. The energy equation is given by Eq. (3), and the viscous work term $\partial[u_i(\tau_{ij} - \rho_f \overline{u_i u_j})]/\partial x_j$ is included to account for the heat generation by viscous dissipation. As mentioned in Sec. 2.1, incompressible multiphase flow, thermal-fluid coupling, and turbulence are included in the fluid domain model. The Euler-Eulerian-based mixture model is adopted for the multiphase flow with cavitation effects. The phase change between liquid and vapor occurs mainly within the fluid-film of unloaded pads or at the leading edge of pads operating in a lubricant starvation condition. Cavitation modeling capability is required for obtaining accurate TPJB response simulations. The mass transfer equation is derived based on the Rayleigh–Plesset model involving bubble dynamics. The continuity equations for the α phase can be written as

$$\frac{\partial}{\partial t}(r_\alpha \rho_\alpha) + \nabla \cdot (r_\alpha \rho_\alpha u_\alpha) = \dot{m}_\alpha \tag{4}$$

The mass transfer equations for evaporation and condensation are

$$\dot{m}_v = C_{F,evap}\frac{3 r_{nuc} r_l \rho_l}{R_{bb}}\sqrt{\frac{2}{3\rho_l}(p_{cav} - p)} \quad \text{(Evaporation)} \tag{5}$$

$$\dot{m}_l = C_{F,cond}\frac{3 r_v \rho_v}{R_{bb}}\sqrt{\frac{2}{3\rho_l}(p - p_{cav})} \quad \text{(Condensation)} \tag{6}$$

where R_{bb} (2 nm), r_{nuc} (5e-4), $C_{F,evap}$ (50), and $C_{F,cond}$ (0.01) are the bubble radius, the volume fraction of nucleation site, the empirical evaporation, and the condensation parameters. The parameters of

the mass transfer equation are obtained via the default values of the CFD solver. The RANS equation produces Reynolds stresses, which are additional unknowns. Therefore, additional equations are needed, and the *k-w*-based SST turbulence model with two additional equations is employed to solve the RANS equation. This is more adaptable to the cases with low Reynolds number than the other two equation models. The turbulent kinetic and frequency equations of the turbulence model are given as Eqs. (7) and (8), respectively.

$$\frac{\partial(\rho_f k)}{\partial t}+\frac{\partial}{\partial x_j}(\rho_f u_j k)=\frac{\partial}{\partial x_j}\left[\left(\mu_f+\frac{\mu_t}{\sigma_{k3}}\right)\frac{\partial k}{\partial x_j}\right]+P_k-\beta'\rho_f k\omega \quad (7)$$

$$\frac{\partial(\rho_f \omega)}{\partial t}+\frac{\partial}{\partial x_j}(\rho_f u_j \omega)=\frac{\partial}{\partial x_j}\left[\left(\mu_f+\frac{\mu_t}{\sigma_{\omega 3}}\right)\frac{\partial k}{\partial x_j}\right]+(1-B_1)2\rho_f\frac{1}{\sigma_{\omega 2}\omega}P_k-\beta_3\rho_f\omega^2 \quad (8)$$

where β' and $\sigma_{\omega 2}$ are 0.09 and 1/0.856, and the coefficients σ_{k3}, $\sigma_{\omega 3}$, and β_3 are determined by linear combinations of the blending functions B_1. In addition to the turbulence model, the gamma transitional turbulence model [24] is included to consider the flow regime transition from laminar (or turbulence) to turbulence (or laminar) near the supply oil inlet in the BP region. A dependent variable of the model is intermittency γ, where the value 1 is considered as fully turbulent and 0 is considered as the laminar flow. The intermittency transport equation is given as follows:

$$\frac{\partial(\rho_f \gamma)}{\partial t}+\frac{\partial(\rho_f u_j \gamma)}{\partial x_j}=\frac{\partial}{\partial x_j}\left[\left(\mu_f+\frac{\mu_t}{\sigma_\gamma}\right)\frac{\partial \gamma}{\partial x_j}\right]+P_{\gamma 1}-E_{\gamma 1}+P_{\gamma 2}-E_{\gamma 2} \quad (9)$$

where the constant σ_γ is typically selected as 1.0 based on empirical results. The source terms of the intermittency equation are mainly functions of the transition onset Reynolds number, which has the default value of 260 from the CFD solver CFX. The turbulent intermittency (*gamma*) interacts with the source term of the kinetic energy equation (7) to predict both laminar and turbulent flow behaviors. The heat transfer problem for the solid domains is also solved in the CFD solver. In the case of the pad domain, only the diffusion term representing heat conduction is taken into account in the energy equation. Unlike the pad domain, the energy equation of the shaft domain also includes an additional convective term for rotational shaft velocity u_s effects. The energy equations for the shaft and pad domains are given below.

$$\text{Shaft:}\quad \frac{\partial \rho_s h_{tot,s}}{\partial t}+\frac{\partial}{\partial x_i}(\rho_s u_s h_{tot,s})=\frac{\partial}{\partial x_i}\lambda_s\frac{\partial T_s}{\partial x_i} \quad (10)$$

$$\text{Pad:}\quad \frac{\partial \rho_p h_{tot,p}}{\partial t}=\frac{\partial}{\partial x_i}\lambda_p\frac{\partial T_p}{\partial x_i} \quad (11)$$

2.3 Pad and Shaft Motions: Search for Equilibrium Position Values. As contrasted with fixed pad bearings, tilting pad bearings allow both static movement and dynamic motion of the pads. The static movement refers to the adjustment in the tilt angle of the pads when the shaft is statically loaded, and the shaft and pad angles converge toward their equilibrium values. Pad dynamic motions occur when the shaft is vibrating due to imbalance or other dynamic loads, and the pads move in response to the shaft's motion. The focus for the following development is the search for the equilibrium positions of the pads and journal, under static loading conditions.

A mesh deformation model is employed to adapt to the shaft and pad motions while prescribing the interface boundaries. The governing equation of the mesh deformation model is as follows:

$$\frac{\partial}{\partial x_i}\Gamma_{dis}\frac{\partial \delta_i}{\partial x_i}=0 \quad (12)$$

where Γ_{dis} is the mesh stiffness, and δ_i is the mesh displacement relative to the previous locations. The conservation of the mesh quality is critical in the thin fluid-film due to its high sensitivity for convergence. Therefore, constant mesh stiffness is selected to maintain the mesh quality by keeping the distances of the mesh nodes through film thickness uniformly.

Figure 3(*a*) illustrates the tilting and pivot motion of a typical node moving at the interface boundaries of pad *j*. The angular position of the pad is caused by the film pressure moment and is the tilting motion that rotates the pad about the *z*-axis of its pivot. The pad can also translate in the pivot direction due to pivot flexibility, and its consideration is required because of its strong effect on the bearing overall stiffness and damping properties [8,25,26]. The pivot displacement of pad *j* in an iteration step is given by Eq. (13), which results from its nonlinear pivot flexibility, as discussed in the literature [26–28].

$$\Delta p_{pvt}{}^j = G_p\sqrt{\frac{C_E{}^2}{K_D}}\left(\sqrt[3]{(F_{p,new}{}^j)^2}-\sqrt[3]{(F_{p,old}{}^j)^2}\right) \quad (13)$$

where $F_p{}^j$ is the applied load on the pad (along the line connecting the bearing center and the pivot), G_p and K_D are geometrical parameters of the pivot and pad, respectively, and C_E is a function of the material properties. The pad and shaft motions occur during the transient movement of the system toward its equilibrium state.

The mesh displacement is imposed at the interface boundaries prior to solving Eq. (12). The pad mesh displacements are derived from the film thickness model, which depends on the pad angles, pivot displacement, and journal position. The Newton–Raphson

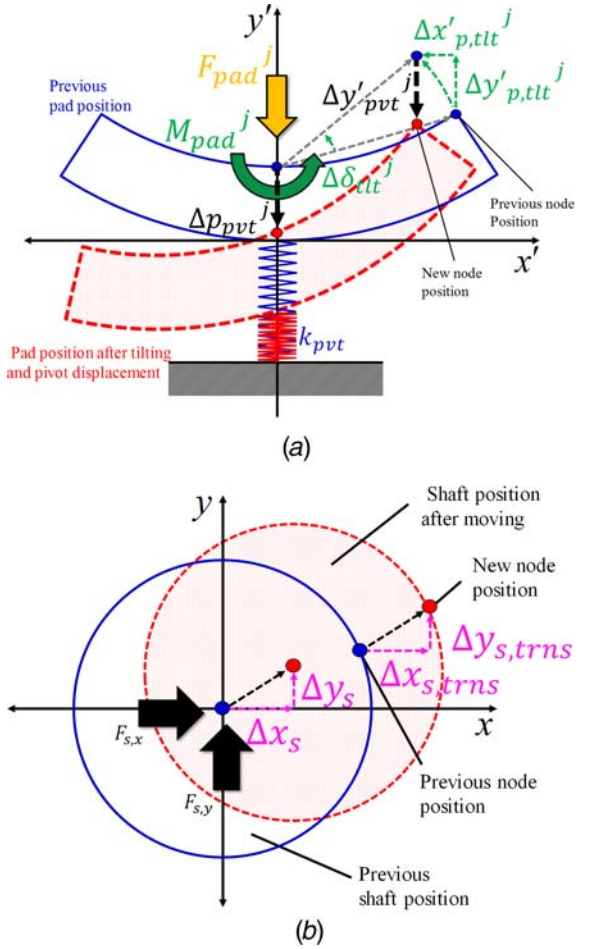

Fig. 3 Illustration of a typical moving node: (*a*) tilting and pivot motion of a pad and (*b*) translational motion of a shaft

method is employed to locate the equilibrium angle of pad j as follows:

$$\Delta\delta_{tlt}{}^{j} = C_{R,p}{}^{j}\frac{\partial\delta_{tlt}{}^{j}}{\partial M_{p}{}^{j}}(M_{trgt}{}^{j} - M_{p}{}^{j}) \tag{14}$$

where $C_{R,p}{}^{j}$ is a relaxation factor, the term $\partial\delta_{tlt}{}^{j}/\partial M_{p}{}^{j}$ is the Jacobian, and the target moment $M_{trgt}{}^{j}$ is zero (at equilibrium). To reduce computation time, the Jacobian is evaluated only once (at the zero pad angle) and is assumed to remain constant throughout the pad angle equilibrium iterations. The initial perturbation angle employed to evaluate the Jacobian can be varied to identify an optimal value for quicker convergence.

The film thickness model is utilized to get the pad mesh displacement, prescribed at the interface boundaries, to preserve the mesh quality without the loss of accuracy. The mesh displacement equation is converted to global x–y coordinates to apply it directly to the CFD solver. Hence, the mathematical relations of the mesh displacement, which are imposed at the interface boundary of pad j can be obtained from the following equations:

$$\Delta x_{p}{}^{j} = \{\Delta x_{p,tlt}{}^{j}\} + \{\Delta x_{p,pvt}{}^{j}\} = \left\{-\frac{\Delta\delta_{tlt}{}^{j}}{R_{s}{}^{2}}x_0(y_0\cos\theta_{p}{}^{j} - x_0\sin\theta_{p}{}^{j})\right\} + \left\{\frac{\Delta p_{pvt}{}^{j}}{R_{s}{}^{2}}x_0(x_0\cos\theta_{p}{}^{j} + y_0\sin\theta_{p}{}^{j})\right\} \tag{15}$$

$$\Delta y_{p}{}^{j} = \{\Delta y_{p,tlt}{}^{j}\} + \{\Delta y_{p,pvt}{}^{j}\} = \left\{-\frac{\Delta\delta_{tlt}{}^{j}}{R_{s}{}^{2}}y_0(y_0\cos\theta_{p}{}^{j} - x_0\sin\theta_{p}{}^{j})\right\} + \left\{\frac{\Delta p_{pvt}{}^{j}}{R_{s}{}^{2}}y_0(x_0\cos\theta_{p}{}^{j} + y_0\sin\theta_{p}{}^{j})\right\} \tag{16}$$

The shaft mesh displacement, which is prescribed at the interface boundary, is obtained in a similar manner as for the pad. As shown in Fig. 3(*b*), a shaft mesh node is moved during the search for the equilibrium position of the shaft, where the applied load and lubricant film pressure-induced load acting on the journal become balanced.

The increment of journal translational position during the Newton–Raphson search for the equilibrium position is obtained from the following equation:

$$\begin{pmatrix}\Delta x_s\\ \Delta y_s\end{pmatrix} = -C_{R,s}\begin{pmatrix}\frac{\partial F_{rct,x}}{\partial x} & \frac{\partial F_{rct,x}}{\partial y}\\ \frac{\partial F_{rct,y}}{\partial x} & \frac{\partial F_{rct,y}}{\partial y}\end{pmatrix}^{-1}\begin{pmatrix}F_{s,x} + F_{rct,x}\\ F_{s,y} + F_{rct,y}\end{pmatrix} \tag{17}$$

(Shaft journal)

where $C_{R,s}$ is the relaxation factor, $F_{rct,x}$ and $F_{rct,y}$ are the reaction forces generated by the fluid-film, respectively, and $F_{s,x}$ and $F_{s,y}$ are the applied loads that are given as input values in the CFD simulation. The Jacobian matrix of Eq. (17) is obtained by imposing small perturbations of journal position in the x and y directions. The shaft mesh displacement is also derived from the film thickness model similar with the pads, and the mathematical relations of the mesh displacement at shaft interface boundaries are given as follows:

$$\Delta x_{s,trns} = \frac{x_0}{R_{s}{}^{2}}(\Delta x_s x_0 + \Delta y_s y_0) \tag{18}$$

$$\Delta y_{s,trns} = \frac{y_0}{R_{s}{}^{2}}(\Delta x_s x_0 + \Delta y_s y_0) \tag{19}$$

2.4 Thermal Deformation of Shaft and Pad (Structural Analysis). The shaft and pads deform due to thermal expansion, which increases with the speed as greater power is dissipated by shearing of the lubricant film, resulting in increasing temperatures. Prior research on TPJB [2,4,6,8] has established the importance of accounting for thermal expansion. Consideration of journal expansion due to centrifugal force is also important due to the very thin film thickness.

The Mechanical APDL code is the FEA solver utilized to solve the linear static structural problem

$$[K][u] = [F^{th}] + [F^{cntr}] \tag{20}$$

for pad and journal displacements, where $[K]$ is the global stiffness matrix, $[u]$ is the nodal displacement vector, $[F^{th}]$ is the thermal load vector, and $[F^{cntr}]$ is the body force vector due to the centrifugal force effect. The pad displacements obtained from the FEA solver are utilized for obtaining the mesh displacement of the interface boundaries in the CFD solver as represented in Eqs. (21) and (22), which are derived from considering the preservation of mesh orthogonal quality.

$$\Delta x_{p,te}{}^{j} = -\frac{x_0}{R_{s}{}^{2}}(\Delta x_{p,TE}{}^{j}x_0 + \Delta y_{p,TE}{}^{j}y_0) \tag{21}$$

$$\Delta y_{p,te}{}^{j} = -\frac{y_i}{R_{s}{}^{2}}(\Delta x_{p,TE}{}^{j}x_0 + \Delta y_{p,TE}{}^{j}y_0) \tag{22}$$

where $\Delta x_{p,TE}{}^{j}$ and $\Delta y_{p,TE}{}^{j}$ are the x and y components of the jth pad displacement solution from the structural analysis. Thus, the total pad displacement vector at the interface boundaries between pad and fluid-film is the summation of the mesh displacement of the pad motion and the thermal deformation as below.

$$[\Delta X_{p,tot}{}^{j}] = [\Delta X_{p}{}^{j}] + [\Delta X_{p,te}{}^{j}] \tag{23}$$

where $[\Delta X_{p}{}^{j}]$ is the jth pad displacement vector due to the pad motion searching for equilibrium and $[\Delta X_{p,te}{}^{j}]$ is the jth pad displacement vector from thermal deformation. Similarly, the shaft (journal) displacement solutions from the FEA solver are applied to interface boundaries of the CFD solver as in Eqs. (24) and (25). Finally, the shaft total displacement vector, due to its translational motion and the thermal deformation, is given in Eq. (26).

$$\Delta x_{s,th} = \frac{x_i}{R_{s}{}^{2}}(\Delta x_{s,TE}x_0 + \Delta y_{s,TE}y_0) \tag{24}$$

$$\Delta y_{s,th} = \frac{y_0}{R_{s}{}^{2}}(\Delta x_{s,TE}x_0 + \Delta y_{s,TE}y_0) \tag{25}$$

$$[\Delta X_{s,tot}] = [\Delta X_{s,trns}] + [\Delta X_{s,te}] \tag{26}$$

where $[\Delta X_{s,trns}]$ is the shaft displacement vector due to its translational motion during the equilibrium condition search, and $[\Delta X_{s,te}]$ is the displacement vector from thermal deformation. The supplementary derivation of the total pad and shaft displacement in Eqs. (23) and (26) are contained in the Appendix. The calculation process of the FSI-CFD model is composed of iterative procedures and continues with transferring the data between the CFD and FEA solvers until the solution converges. The details are represented in Sec. 2.6.

2.5 Boundary Condition. The governing equations are solved while satisfying the boundary conditions presented in Fig. 4 and Table 1. Lubricant oil is supplied at the supply oil inlet (7) and flows to the oil side outlet (9), while moving with shaft drag and pressure forces in the fluid-film domain. The inlet and outlet are described by open boundary conditions with a prescribed supply pressure, which may have recirculation flow, if it occurs. It is assumed that only the liquid phase exists at the inlet and outlet of the fluid-film domain, which implies that the liquid phase volume fraction is 1 at these locations. The turbulence intensity value has only a minor effect on the desired responses and is assigned a value of 5% (medium) at both the inlet and the outlet, which implies that the turbulence intensity $\left(\sqrt{2k/(3u^2)}\right)$ is 0.05 and the viscosity ratio (μ_t/μ, $\mu_t = \rho k/\omega$) is 10. The turbulence intermittency is selected to be consistent with the given turbulence intensity at the inlet and outlet of the

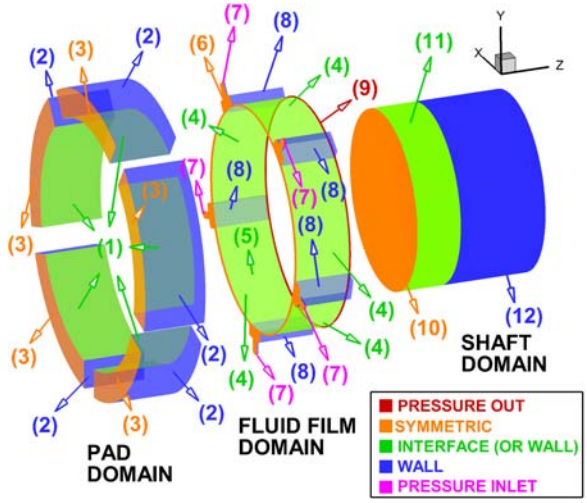

Fig. 4 Boundary conditions imposed in the TPJB model

fluid-film domain and is set to zero (laminar) on the walls for consistency with the selected turbulence intensity.

The surfaces between the fluid-film and shaft domain (11) and between the fluid-film and pad domains (12) are prescribed with interface boundaries that enforce the continuity of dependent variables and their gradients in each domain at surfaces facing each other. Shaft rotational motion (spin) is applied at the shaft–fluid interface with moving wall velocity conditions. The mesh displacements determined by Eqs. (23) and (26) are imposed at the fluid–pad interface and shaft–fluid interface, respectively, for calculating the mesh deformation by the shaft-pad motion and thermal deformation. For thermal boundary conditions, both the inlet and outlet temperatures are maintained at 40 °C, all walls have a heat transfer coefficient of 50 W/m^2, and the ambient temperature is 30 °C, except for the surface between pads (8) which is applied as an adiabatic condition. Pad and shaft symmetry at the midplane (10) of the journal and pads is imposed with fixed displacement in the z-direction and free displacements in the x–y directions, for the FEA solver. In addition, the x–y fixed and z free boundary conditions are applied in a line on the pivots of the pads and on the center nodes of the shaft [8] for thermally induced deformations.

2.6 Calculation Procedure. This section provides an in-depth discussion of the calculation procedure for the FSI-CFD modeling of a TPJB for static performance prediction. Figure 5 shows a flow chart for the simulation procedure. The CFD solver starts by initializing the dependent variables. In the details, the fluid velocity in the circumferential direction is 80 m/s, and the other velocity components are 0 m/s. The static pressure is initialized with 0.5 MPa. The fluid consists of the only liquid phase, and the turbulence intensity is 5% in the full fluid domain at the initial stage. The fluid-film, pad, and shaft temperatures are initialized with 80, 80, and 60 °C, respectively. The mesh deformation equation is then solved using the mesh displacements imposed at the interface boundaries. The wall scale, which is the nearest node to the wall boundary, is utilized in solving the turbulence equation. The velocity, volume fraction, and temperature for the fluid-film and solid domains are then solved in that order.

One iteration of the false time is performed once the turbulence equation is calculated. After the one iteration is completed in the CFD solver, the process proceeds to obtain the mesh displacement prescribed at the interface boundaries as described in Sec. 2.5. Extensive simulation studies revealed that convergence problems occur when the mesh displacements of the shaft and pads are updated for all iterations. It was determined that reducing the update frequencies for the mesh displacement of the pad tilting, pivot, and shaft translational motion improved convergence significantly. Figure 5 shows that the mesh displacement for the pad tilting, shaft translational, and pivot motions is recommended to be updated once every 20, 100, and 500 CFD solution iterations, respectively. The updated frequencies are determined empirically and are adjustable according to the case studied. Similarly, the mesh displacement resulting from thermal deformation is updated with a reduced frequency, which also differs from the shaft and pad motion mesh displacement update frequencies. The CFD solver is interrupted, and the CFD solution is transferred to the FEA solver for the structural analysis, when the accumulated iterations become multiples of one thousand. The updated mesh displacement results from the thermal deformation are transferred to the CFD solver to update its mesh displacement at interface boundaries. The calculations then continue until (a) the dependent variables satisfy the convergence criteria that the residuals of all dependent variables should be below 1.E-6 except for the turbulence intermittency (1.E-5) and (b) the degree of variation of the 500 iteration-averaged monitored parameters, such as load carrying capacity, drag torque, and supply oil flow rate, is below 0.5%.

3 Description of Reynolds Model

A conventional Reynolds model for TPJB response is employed for comparing with the newly developed CFD-based model. Special cases are modeled to produce results that should have the close agreement between CFD and Reynolds, as a check on the CFD model. The Reynold's results are obtained from an in-house code, which is widely used for modeling TPJBs, has low computational load, and has verified accuracy [8]. The Reynolds model has almost equivalent modeling capabilities with regard to its modeling of domain and analyses, including thermal deformation and pivot flexibility capabilities. The Reynolds model is simplified relative to CFD in that it is derived by combining the continuity and simplified momentum equations into a single pressure-based governing equation, while also imposing flow assumptions in the film and in

Table 1 Boundary conditions imposed in the TPJB model

No.	Description	B.C type (CFD)	B.C type (FEA)
1	Pad (1)-Fluid (4) interface	(1)–(4) interface,[a] convection	—
2	Pad outer surface (2)	Convection	Displacement in a line on pivot x, y: fixed, z: free
3	Pad symmetry (3)	Zero z heat flux	Displacement x, y: free, z: fixed
4	Shaft (5)–fluid (11) interface	(5)–(11) interface[a]	—
5	Fluid symmetry (6)	Zero z gradients	—
6	Supply oil inlet (7)	Pressure prescribed	—
7	Surface between pads (8)	Adiabatic	—
8	Oil side outlet (9)	Pressure prescribed	—
9	Shaft symmetry (10)	Zero z heat flux	Displacement x, y: free, z: fixed
10	Shaft outer surface (12)	Convection	—

[a]Interface implies continuity of temperature and flux

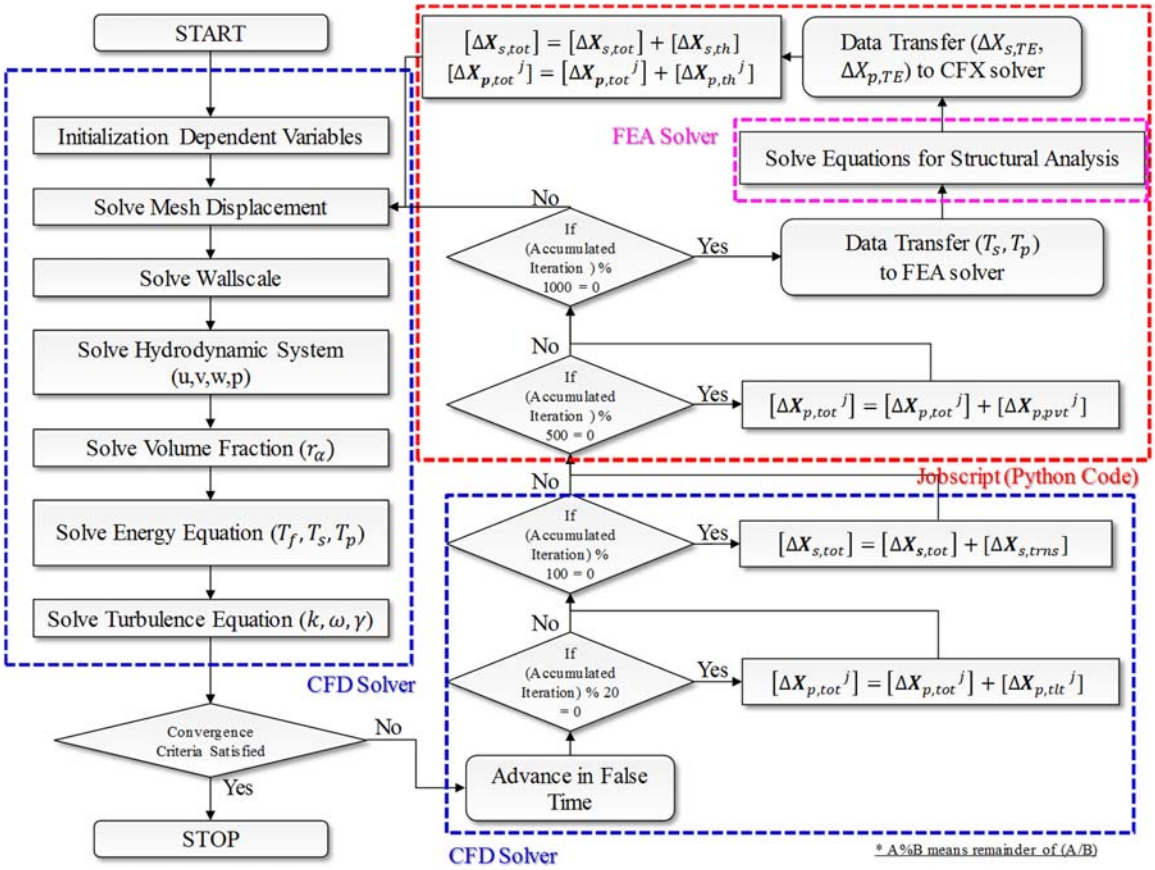

Fig. 5 FSI-CFD TPJB modeling procedure for the static response

the between pads BP regions with mixing theory. The generalized Reynolds equation, which includes variable viscosity through the film thickness, is given by the following equation:

$$\nabla \cdot (D_1 \nabla p) + (\nabla D_2) \cdot \boldsymbol{U}_s + \frac{\partial h}{\partial t} = 0 \tag{27}$$

where

$$D_1 = \int_0^h \int_0^z \frac{\xi}{{}_0\mu_f} d\xi dz - \frac{\int_0^h \frac{\xi}{{}_0\mu_f} d\xi}{\int_0^h \frac{1}{{}_0\mu_f} d\xi} \int_0^h \int_0^z \frac{1}{{}_0\mu_f} d\xi dz \tag{28}$$

$$D_2 = \frac{\int_0^{h_f} \int_0^z \frac{1}{{}_0\mu_f} d\xi dz}{\int_0^{h_f} \frac{1}{\mu_f} d\xi} \tag{29}$$

The three-dimensional energy equation for the Reynolds model is as follows:

$$\rho_f C_{p,f} \left(\frac{\partial T_f}{\partial t} + U \frac{\partial T_f}{\partial x} + W \frac{\partial T_f}{\partial z} \right) = k_f \left(\frac{\partial^2 T_f}{\partial x^2} + \frac{\partial^2 T_f}{\partial y^2} + \frac{\partial^2 T_f}{\partial z^2} \right) + \mu_f \left[\left(\frac{\partial U}{\partial y} \right)^2 + \left(\frac{\partial W}{\partial y} \right)^2 \right] \tag{30}$$

where T_f is the fluid temperature, U and W represent the circumferential and axial flow velocities across film thickness, respectively, and $\boldsymbol{U}_s$ is the shaft velocity vector. The heat generation source term $\mu_f[(\partial U/\partial y)^2 + (\partial W/\partial y)^2]$ is included in the energy equation (30), as is the diffusion term, which accounts for heat conduction, but is typically negligible except for in the film thickness direction. The film thickness h^j corresponding to the jth pad is given by the following equation:

$$h^j = C_{l,p}{}^j - \{x_s - p_{pvt}{}^j \cos(\theta_p{}^j)\} \cos(\theta) - \{y_s - p_{pvt}{}^j \sin(\theta_p{}^j)\} \sin(\theta) - (C_{l,p}{}^j - C_{l,b}) \cos(\theta - \theta_p{}^j) - \delta_{tlt}{}^j R_s \sin(\theta - \theta_p{}^j) - h_{s,TE} - h_{p,TE} \tag{31}$$

where $\delta_{tlt}{}^j$ is the rotation angle of the jth pad, $p_{pvt}{}^j$ is the pivot displacement of the jth pad relative to its pivot initial location, $\theta_p{}^j$ is the center angle of the jth pad, and x_s and y_s are the x and y shaft displacements, respectively, relative to the bearing center. The same boundary conditions are applied on the CFD and Reynolds models as a comparison validation step before considering the actual complex flow patterns that occur in the BP regions. In this simplified model step, additional equations for approximating the lubricant's temperature at the leading edge of pads are employed. These equations are derived from mixing theory as proposed by Suh and Palazzolo [8]:

$$T_{in}{}^j = \begin{cases} \dfrac{Q_{out}{}^{j-1} T_{out}{}^{j-1} + (Q_{in}{}^j - Q_{out}{}^{j-1}) T_{sup}}{Q_{in}{}^j} & \text{if } \mathrm{MC} \cdot Q_{in}{}^j > Q_{out}{}^{j-1} \\ \dfrac{\mathrm{MC} \cdot Q_{in}{}^j T_{out}{}^{j-1} + (Q_{in}{}^j - MC \cdot Q_{in}{}^j) T_{sup}}{Q_{in}{}^j} & \text{if } \mathrm{MC} \cdot Q_{in}{}^j \le Q_{out}{}^{j-1} \end{cases} \tag{32}$$

where $Q_{in}{}^j$ and $Q_{out}{}^{j-1}$ are the inflow rate of pad j and outflow rate of pad $(j-1)$, respectively, $T_{out}{}^{j-1}$ is the temperature at the outlet of pad $(j-1)$, and the MC is constant and typically

determined empirically. The MC can be expressed by rearranging Eq. (32) as

$$\mathrm{MC} = \frac{T_{in}{}^{j} - T_{sup}}{T_{out}{}^{j-1} - T_{sup}} \begin{cases} = \dfrac{Q_{out}{}^{j-1}}{Q_{in}{}^{j}} & \text{if } \mathrm{MC} > \dfrac{Q_{out}{}^{j-1}}{Q_{in}{}^{j}} \\ = 0.4\text{–}1.0 & \text{if } \mathrm{MC} \le \dfrac{Q_{out}{}^{j-1}}{Q_{in}{}^{j}} \end{cases} \tag{33}$$

The finite element method, including an upwind scheme to treat the convection term in Eq. (30), is employed to solve the Reynolds model. A higher fidelity CFD model, which includes the complex 3D flow between pads, is presented in Sec. 4 for the initial CFD—Reynold comparison.

4 Comparison of Computational Fluid Dynamics and Reynolds Models Results

Simulations for the CFD and Reynolds model were conducted for "with mixing effect" and "without mixing effect," including the following additional conditions *(a) rigid pivots and no thermal deformations, (b) flexible pivots, and (c) flexible pivots and thermal deformations*. All cases take into account shaft translations and pad tilting motion in the equilibrium state search process.

4.1 Input Conditions. Figure 6 shows the geometry of a representative TPJB utilized in the simulations. The input parameter values for the model are listed in Table 2. This includes both fluid properties needed for modeling the fluid domain and solid properties required for calculating the temperature and thermal deformation of the solid domains.

Figure 7 shows the fluid and solid domains and their corresponding mesh patterns. The fluid-film domain's mesh has a global element size of 0.75 mm and 12 layers of elements through the film thickness. Maintaining a close first node distance from the interface boundaries is critical for accurate turbulence modeling and is kept at 0.1 μm from grid tests. Elements are uniformly spaced through the film thickness. Figure 7(*c*) shows that the shaft mesh is made with a low-density uniform ten layers in the radial direction and a smaller layer thickness mesh near the outer surface of the shaft. The lower density meshing lowers the computational load without significant loss in accuracy because of the corresponding low gradients in the dependent variables. The size of the shaft mesh contacting the fluid-film domain in the circumferential and axial directions is consistent with that of the fluid-film domain for the exact interpolation at the interface boundaries.

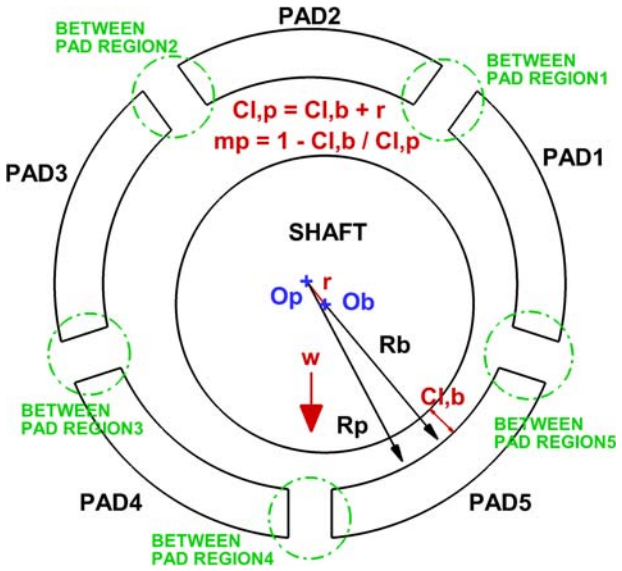

Fig. 6 Geometry of example tilting pad journal bearing TPJB

Table 2 Input parameters

Parameters	Symbol	Value
Shaft diameter (mm)	D_b	101.6
Bearing length (mm)	L_b	50.8
Bearing clearance (mm)	C_b	0.0749
Number of pads	N_{pad}	5
Pad thickness (mm)	t_{pad}	12.7
Pad offset	β	0.5
Pad arc length (deg)	l_{pad}	60
BP height (mm)	H_{bp}	5.2
BP nozzle hydraulic diameter (mm)	D_{bp}	1.8
BP seal radial clearance (mm)	h_{bp}	0.425
Applied load (N)	w	5000
Preload	m_p	0.5
Operating speed (rpm)	Ω	3000–15,000
Supply pressure (kPa)	P_{in}	132
Fluid property, ISO 32		
Liquid density (kg/m^3)	ρ_l	860
Liquid viscosity (Pa · s)	μ_l	$0.03424e^{-0.0304(T_f - T_{ref})}$
Liquid specific heat (J/kg°C)	$C_{p,l}$	2000
Liquid heat conductivity (W/mK)	λ_l	0.133
Vapor density (kg/m^3)	ρ_v	0.029
Vapor viscosity (Pa · s)	μ_v	9e-6
Vapor specific heat (J/kg°C)	$C_{p,v}$	1000
Vapor heat conductivity (W/mK)	λ_v	0.026
Cavitation pressure (kPa)	P_{cav}	−90
Solid property, steel (pad, shaft, and pivot)		
Density (kg/m^3)	ρ_s	7850
Specific heat (J/kg°C)	$C_{p,s}$	434
Heat conductivity (J/m°C)	λ_s	60.5
Young's modulus (Pa)	E_s	2.1×10^{11}
Poisson's ratio	ν_s	3.0
Thermal expansion coefficient (1/°C)	α_s	1.1×10^{-5}
Reference temperature (°C)	T_{ref}	30
Pivot configuration		
Circumferential radius (pivot), (mm)	R_{p1}	56
Axial radius (pivot) (mm)	R_{p2}	56
Circumferential radius (housing) (mm)	R_{h1}	−57.15
Axial radius (housing) (mm)	R_{h2}	∞

The pad mesh is generated to have the same volumetric element size with the fluid domains to properly implement the interpolation of dependent variables at the interface boundaries between the pad and fluid-film domains.

Although the CFD model is mathematically more complex than the Reynolds model, the Reynolds model still has a high degree of accuracy when neglecting the BP flow and heat transfer. This results from highly accurate, thin film assumptions inherent in the Reynolds equation's derivation. The major difference between the CFD and the Reynolds model is the high fidelity of modeling with CFD in the BP regions. The CFD model encompasses the 3D fluid dynamic behavior between pads, including turbulence, multiphase flow, and heat transfer. The Reynolds model assumes complete mixing between the pads as expressed in Eq. (32) and depends mainly on an empirically derived MC.

The CFD and the Reynolds approaches do not explicitly model the BP region in this section. This is referred to as the "without mixing effect" case. It is expected that the CFD and Reynolds approaches should have a reasonable agreement because the inertia effect, radial pressure gradient, and shaft curvature effect are negligible in the pad region. Thus, the CFD model can be validated by comparing it to the Reynolds model, without the mixing effect. Both models are later compared while including the mixing effect in Sec. 4.3.

Figure 8 shows the BP models for the "without mixing effect" and the "with mixing effect" conditions. The CFD model has a prescribed constant temperature and constant pressure boundaries

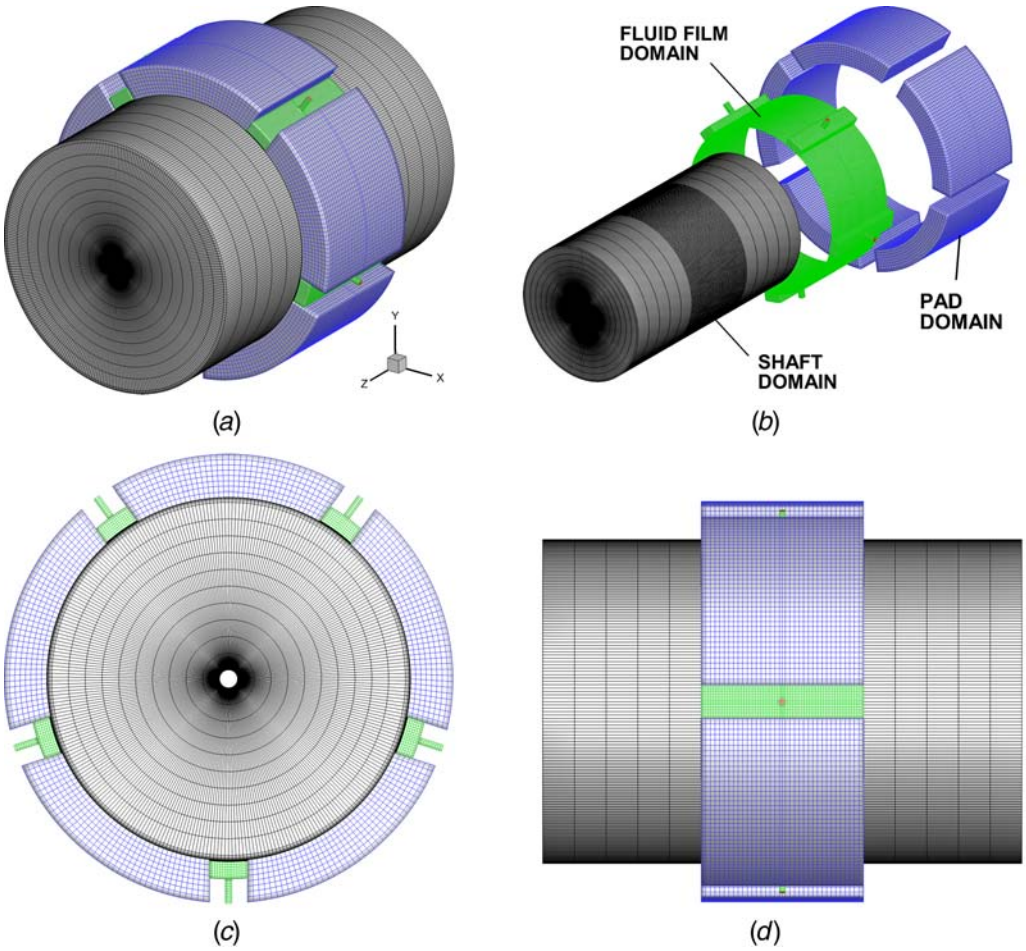

Fig. 7 Geometry and mesh of example TPJB: (*a*) overview (427,558 elements), (*b*) exploded view (scaled factor; shaft 0.7, fluid-film 0.9), (*c*) *x–y* view, and (*d*) *x–z* view

between the pads for the "without mixing effect" case as shown in Fig. 8(*a*). The CFD model includes an oil injection subdomain for the "with mixing effect" as shown in Fig. 8(*b*). The Reynolds model employs an MC equal to zero for the "without mixing effect" cases and 0.4–1.0 for the "with mixing effect" cases. The CFD and the Reynolds models results are compared for validation of the CFD approach.

4.2 Comparison of Computational Fluid Dynamics and Reynolds for "Without BP Mixing" Model. The simulation results for the "without mixing effect" condition are presented in this section and are obtained from CFD and Reynolds models, the latter employing both 3D and 2D energy equation solutions in the fluid-film. The Reynolds model is well known to provide accurate results in the thin film regions of the pads but is incapable of modeling the relatively large, complex flow region between pads BP. Modeling of only the pad thin film regions provides an opportunity to validate the CFD results by comparison with the Reynolds results for pressure/force, temperature, and equilibrium position results. Comparisons between the models are made for the three cases: *case A, rigid pivots and no thermal deformations; case B, flexible pivots; case C, flexible pivots and thermal deformations*. The pressure and thermal boundaries are applied identically in both models: pressure at the leading, trailing, and side edge is 132, 132, and 0 kPa, and the temperature at all edges is 40 °C. Boundaries of the shaft and pad are convection with the heat transfer coefficient of 50 W/m^2. Finally, the ambient temperature is 30 °C. The results are shown in Figs. 9–11, where the symbols indicate the Reynolds model results with 3D and 2D energy equations, and the lines indicate the CFD model results. The 2D energy equation neglects temperature variations in the axial direction and generally executes much faster than the 3D energy equation model. The eccentricity ratio as shown in the results is defined as the static offset of the journal divided by the radial bearing clearance.

The above results clearly show the close agreement between the CFD and Reynolds (2D and 3D) predictions. The 2D Reynolds and 3D Reynolds have very close agreement due to the very small gradient of temperature in the majority of the axial direction. This provides an initial validation of the CFD approach for the simplified (without mixing effect) pad-only model. Some trends noted in the above results include: (1) attitude angle, drag torque, side leakage, and shaft and pad temperatures increase, and eccentricity decreases with the increasing speed (rpm), (2) inclusion of pivot flexibility results in increased eccentricity and decreased drag torque and shaft and pad temperatures, and (3) inclusion of pivot flexibility plus thermal expansion results in increased drag torque, side leakage, and shaft and pad temperatures and decreased eccentricity ratio.

4.3 Comparison of Computational Fluid Dynamics and Reynolds for "With BP Mixing" Model. The simulation results for the "with mixing effect" condition are presented in this section and are obtained from CFD and Reynolds models, the latter employing a 3D energy equation solution in the fluid-film and incorporating an MC to account for the mixing of carryover and supply oil between pads. Comparisons between the models are made for the three cases: *case A, rigid pivots and no thermal deformations; case B, flexible pivots; case C, flexible pivots and thermal deformations*. The pressure and thermal boundary

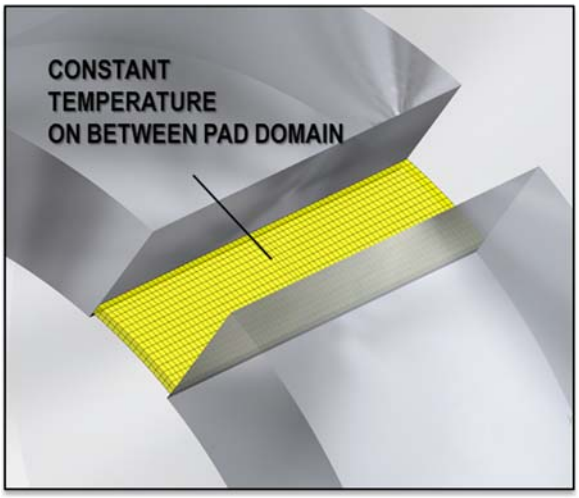

(a)

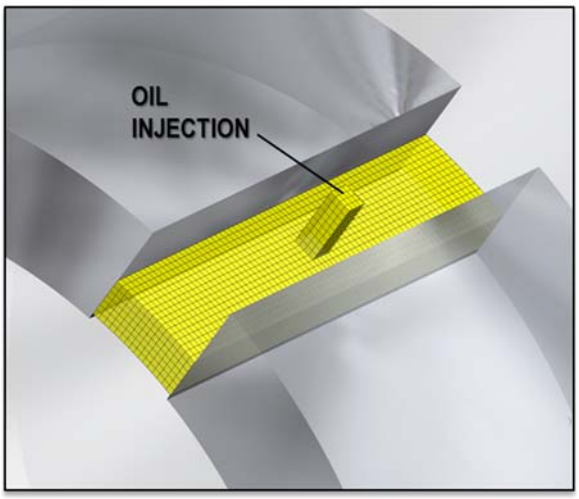

(b)

Fig. 8 BP subdomain CFD model for the "with and without mixing effect" cases: (*a*) without mixing effect and (*b*) with mixing effect

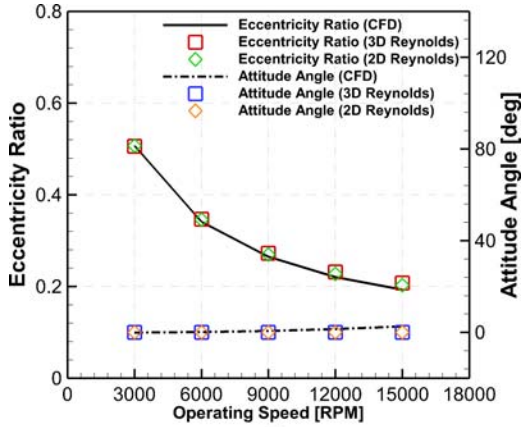

(a)

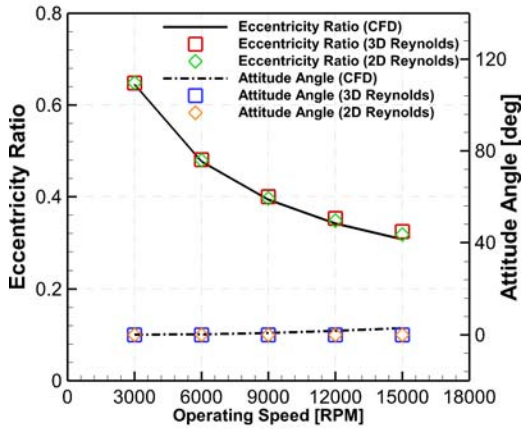

(b)

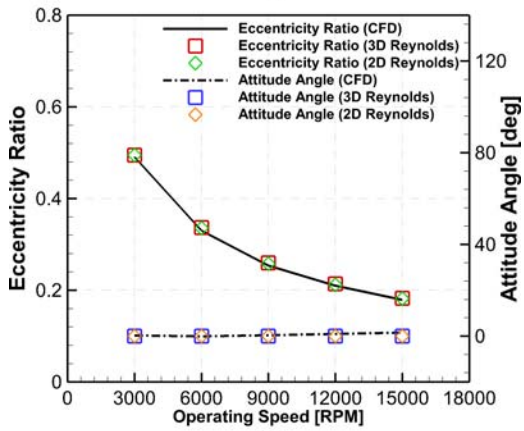

(c)

Fig. 9 Eccentricity and attitude angle for "without mixing effect" model and (*a*) case A, (*b*) case B, and (*c*) case C effects

conditions are the same as described in Sec. 4.2, except for the pad inlet temperature of the BP region. For the Reynolds model, the pad inlet temperature of the BP is determined by the mixing theory as represented in Eq. (32). The CFD considers BP including oil injection with the supply pressure 132 kPa, and the temperature field of BP region is obtained by solving the governing equations of CFD.

Figure 12 shows that the eccentricity ratio is very sensitive to the selection of the MC in the Reynolds model for case A and case B, based on the eccentricity plots versus speed for MC = 0.4 and 1.0. The plots show that the Reynolds model with MC = 0.4 has an eccentricity close to the CFD prediction for low rpm, but the CFD eccentricity moves closer to the Reynolds MC = 1.0 as rpm increases. This suggests that a speed-dependent MC should be utilized in a Reynolds model. The CFD results fall within the range of the MC results, indicating that the Reynolds model has the potential for matching CFD model results; however, only if accurate, speed-dependent MCs are incorporated in the Reynolds model. The sensitivity of the eccentricity ratio to MC in the Reynolds model is negligible for case C, and agreement between Reynolds and CFD is close but increasingly deviates with an increasing rpm.

Figure 13 shows a high sensitivity of equilibrium position attitude angle to Reynolds model MC for all three cases A, B, and C. As shown in Fig. 12, the plots indicate that a speed-dependent MC would be required for the Reynolds model to match the CFD model results. Drag torque is plotted versus rpm for the Reynolds and CFD models in Fig. 14. The shear stress is defined from the dynamic viscosity (μ) and the gradient of tangential velocity (u_{tmg}) at shaft surface, and the drag torque is obtained by integrating the product of shaft radius and shear stress at shaft surface as

$$DT = \int_{A_s} (R_s \times \mu \frac{\partial u_{tmg}}{\partial r}) dA_s$$

The Reynolds approach excludes drag losses between pads BP, so only the on-pad contributions to the drag torque are plotted. The CFD approach includes a detailed model of the BP flows and heat transfer, so both BP and on-pad drag torque contributions are plotted. The total drag torque is the sum of the on-pad and BP

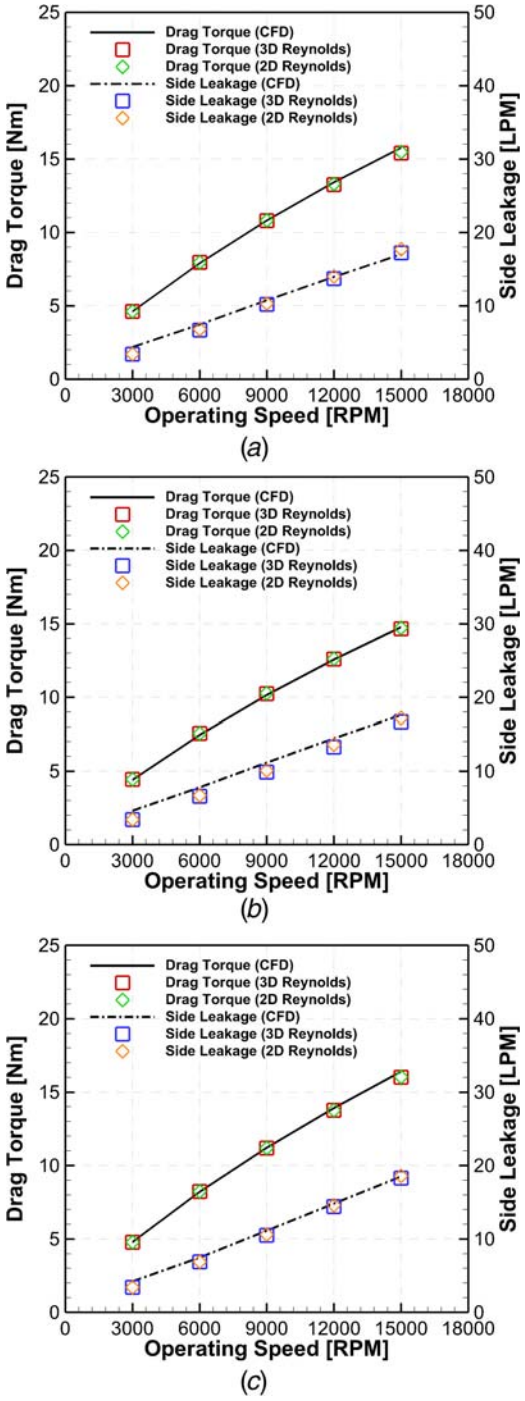

Fig. 10 Drag torque and side leakage for "without mixing effect" model and (*a*) case A, (*b*) case B, and (*c*) case C effects

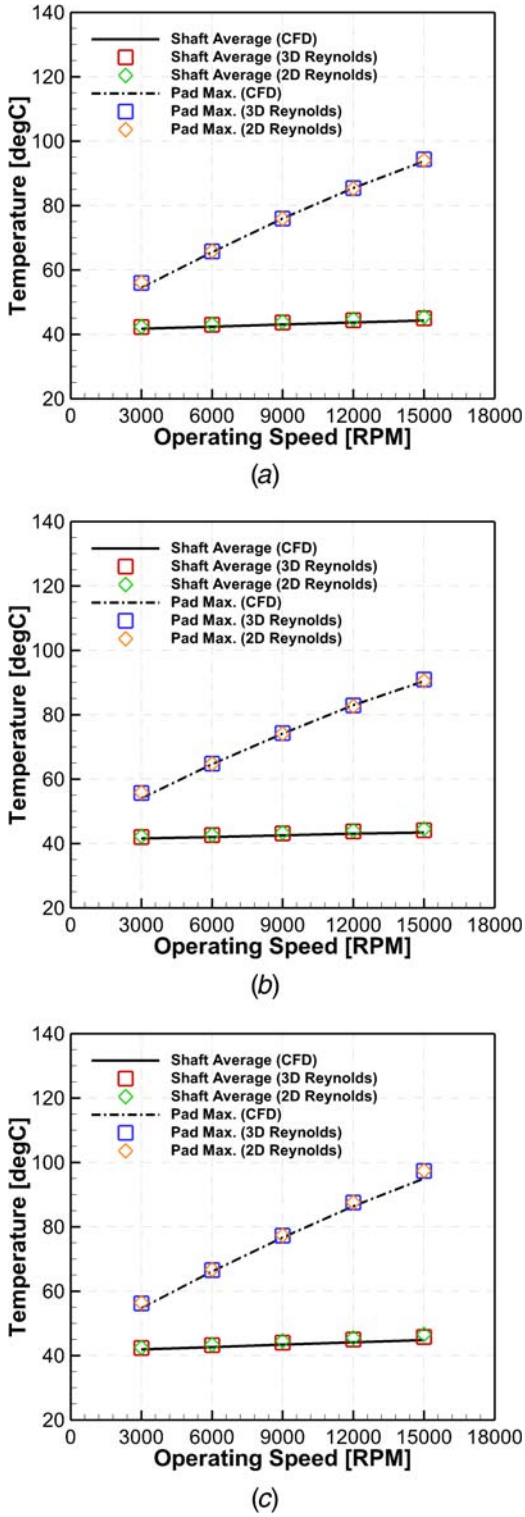

Fig. 11 Shaft average and pad maximum temperature for "without mixing effect" model and (*a*) case A, (*b*) case B, and (*c*) case C effects

contributions. The CFD results show that the BP contribution to drag torque is significant reaching a maximum of 13% of the total drag torque at the highest rpm modeled. A wide variation of drag torque prediction with MC is noted for the Reynolds model, which increases with rpm. The MC = 0.4 results show better agreement with CFD over the range of rpm considered; however, an even smaller MC would be required to match the total drag torque prediction of the CFD model for all three cases A, B, and C.

Figure 15 shows that the side leakage on the pads is fairly insensitive to MC in the Reynolds model, and agrees very well with CFD for cases A and B, but deviates significantly above 9000 rpm for case C. The supply oil flow rate, which is equal to the summation of the flow between pads and on pads, is increased with the increase of the operating speed. The side leakage on the pads is seen to decrease in the CFD model when the thermal growth of the pad is included, which results in a thinner film on the pads. The BP side leakage dominates on the pad side leakage at low speeds, but the differences between the two leakage types diminish as speed increases. This results from the supply pressure driving significant flow at low speeds in the model, and most of the flow becomes side leakage BP.

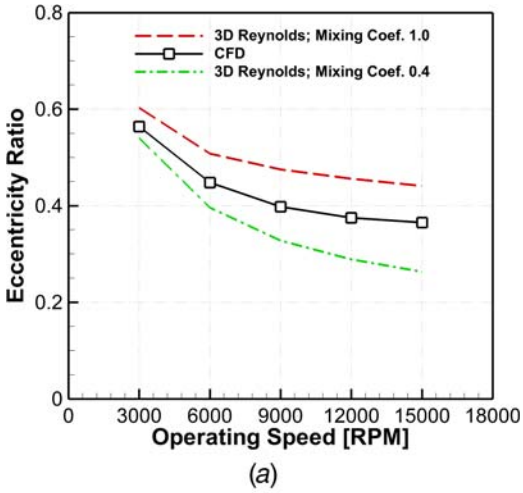

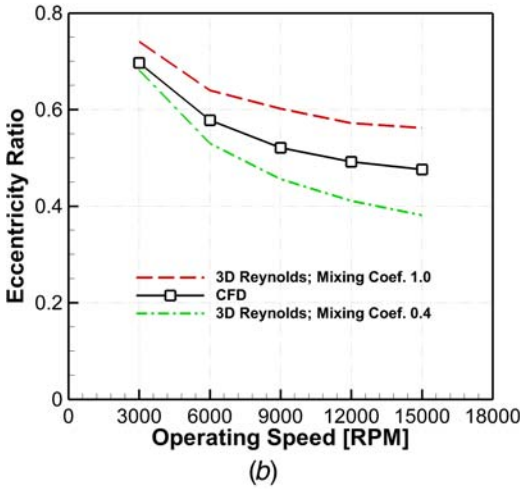

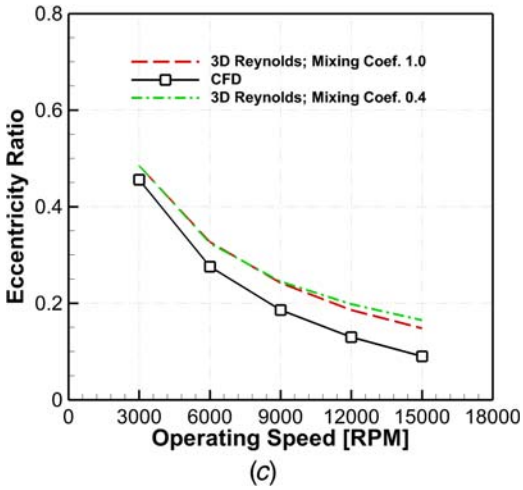

Fig. 12 Eccentricity for "with mixing effect" model and (*a*) case A, (*b*) case B, and (c) case C effects

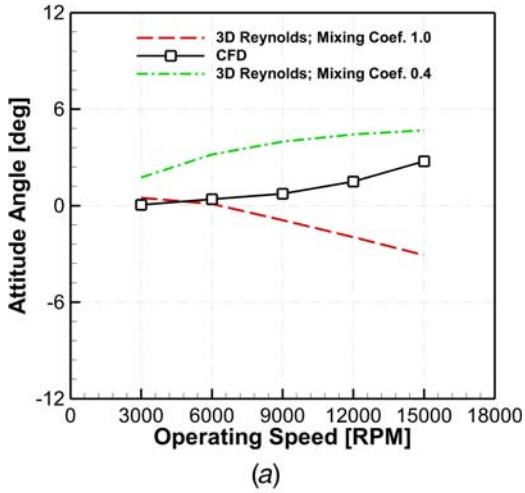

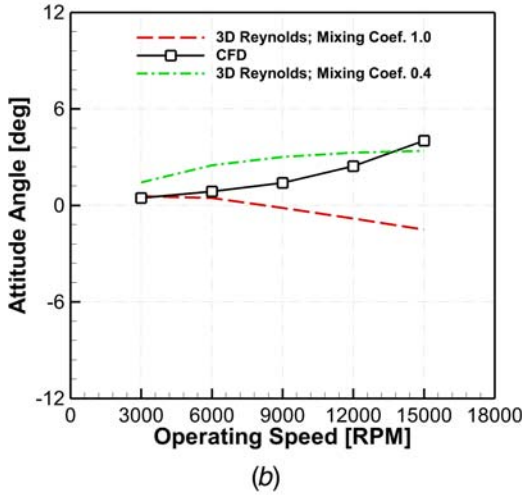

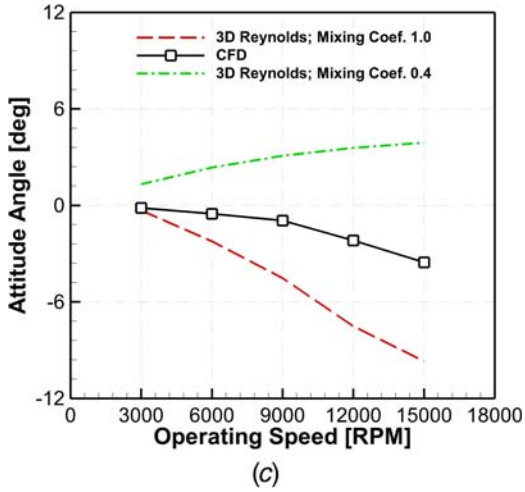

Fig. 13 Attitude angle for "with mixing effect" model and (*a*) case A, (*b*) case B, and (c) case C effects

Figure 16 shows a high sensitivity of volumetric average shaft temperature to MC in the Reynolds model, with a maximum deviation of 26.8 °C between the MC = 0.4 and the MC = 1.0 cases. The agreement between CFD and the MC = 1.0 Reynolds model is good.

Figure 17 again shows a high sensitivity of the Reynolds model predictions to MC value, in this case for the pad maximum temperature (hot spot). Contrary to the shaft average temperature in Fig. 16, the CFD results are nearest to the Reynolds MC = 0.4 extreme case, instead of the Reynold MC = 1.0 extreme case. The CFD predictions are seen to fall within the MC = 0.4 and MC = 1.0 predictions for the Reynolds model for case C, unlike the shaft temperature where the CFD prediction is above both MC value predictions. These results show that a choice for MC may provide highly accurate results for one response variable but much less accurate results for another response variable, assuming that the CFD results provide a benchmark for high accuracy.

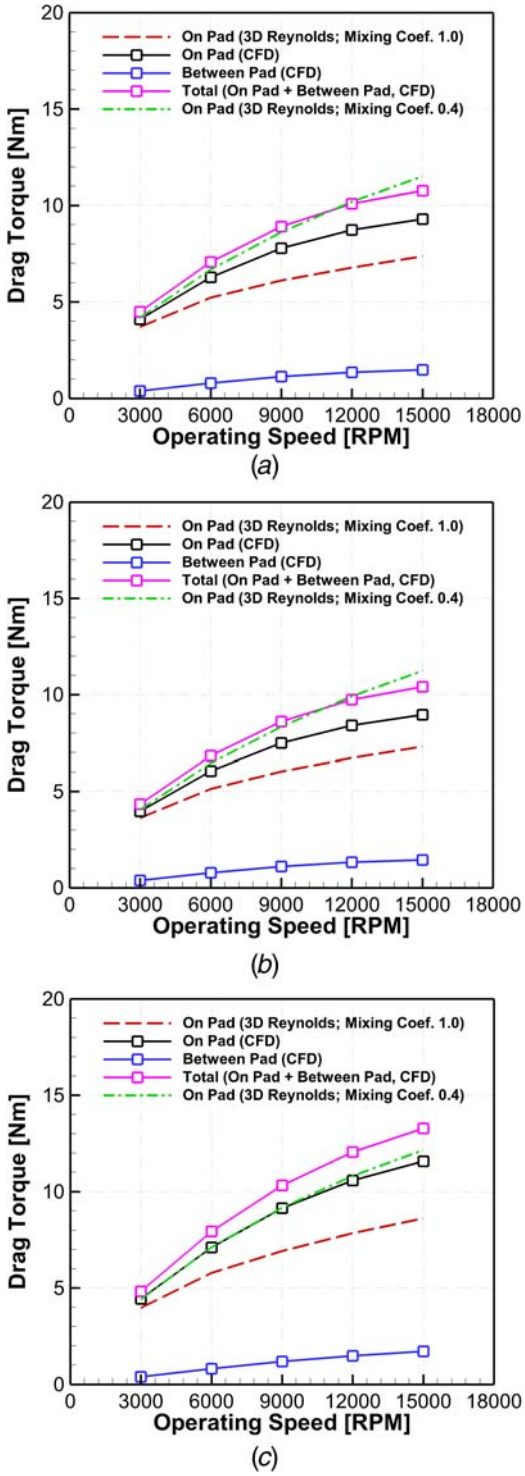

Fig. 14 Drag torque for "with mixing effect" model and (*a*) case A, (*b*) case B, and (*c*) case C effects

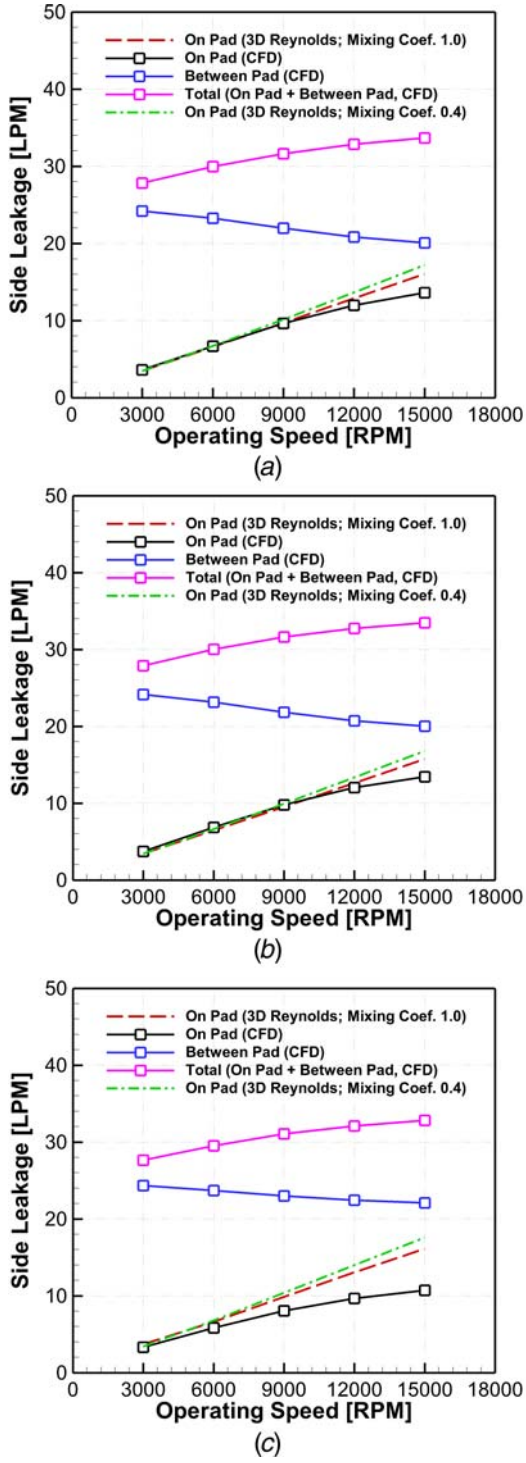

Fig. 15 Side leakage of "with mixing effect" condition: (*a*) case A, (*b*) case B, and (*c*) case C

Comparison with the CFD results reveals that the mixing theory of the Reynolds model ignores the MC variation in the axial direction and temperature variation in the radial direction at the inlet of the pads. The assumption of a constant MC in the axial direction and uniform temperature through the film thickness at a pad leading edge leads to inconsistency in the response variable predictions when comparing CFD and Reynolds model results in Figs. 12–17. For example, the Reynolds (MC = 0.4) model severely underpredicts the shaft average temperature in Fig. 16, which may lead to a significantly larger operating clearance, which might affect operating eccentricity, pad temperatures, stiffness, and damping.

Figures 18 and 19 show response variable (pressure, shear stress, and heat flux) contours predicted by CFD for operating speeds of 3000 rpm and 15,000 rpm, respectively. Both flexible pivots and thermal deformations (case C) are included in the model. Figures 18(*a*) and 19(*a*) show that the pressure increases from the leading edge and decreases approaching the trailing edge after reaching a maximum point. The pressure is generated mainly in the lower pads at 3000 rpm. The pressure in the upper pads

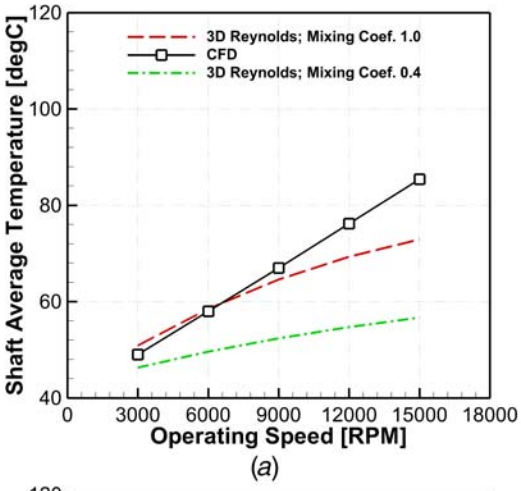

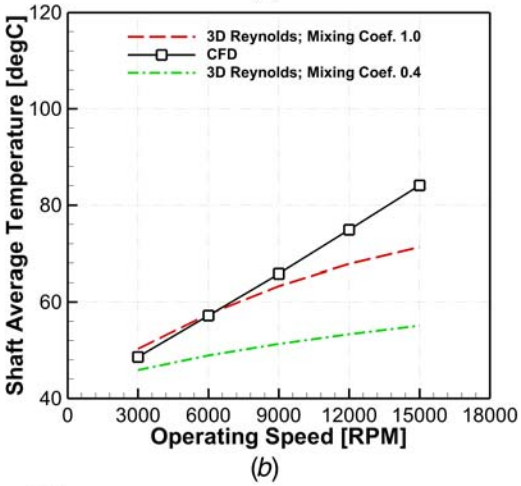

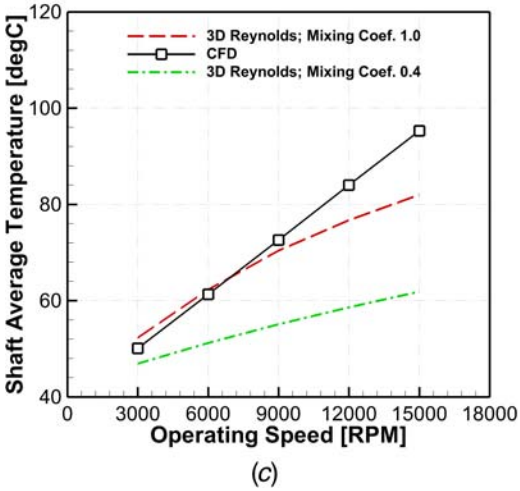

Fig. 16 Shaft average temperature of "with mixing effect" condition: (*a*) case A, (*b*) case B, and (*c*) case C

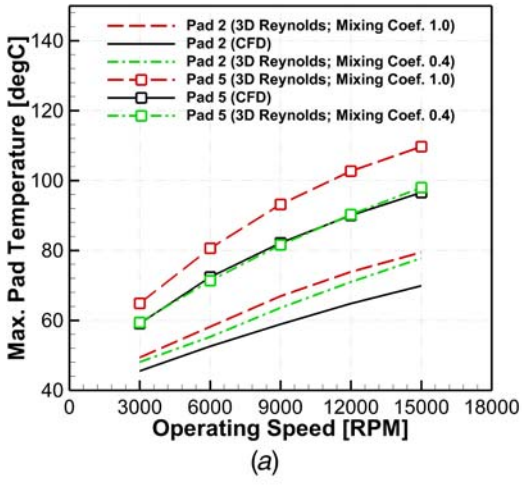

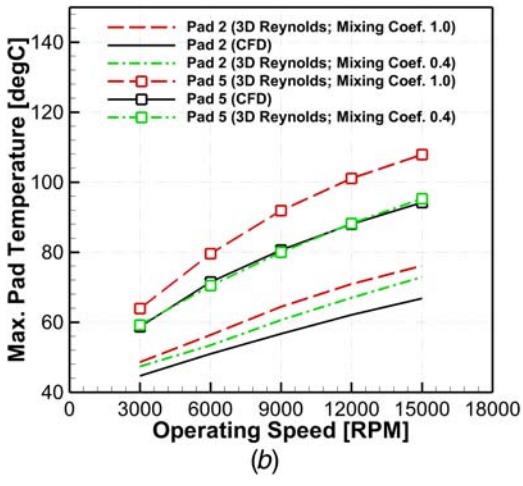

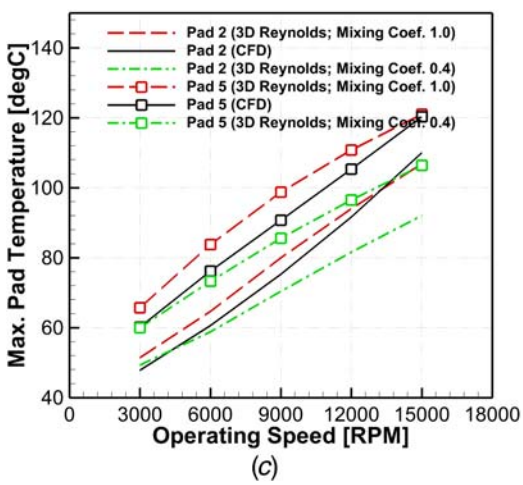

Fig. 17 Maximum pad temperature of "with mixing effect" condition: (*a*) case A, (*b*) case B, and (*c*) case C

increases with the speed, which causes a lowering of the eccentricity, i.e., a centering of the shaft.

Figures 18(*b*) and 19(*b*) show shear stress contours that increase with the increasing shaft speed. Shear stress occurring in the BP regions becomes more significant in the high operating speed condition. Shear stress is principally a function of the pressure gradient, operating speed, and film thickness in the Reynolds model, and the CFD results follow these trends. For instance, higher shear stress occurs where the pressure is increased and decreases due to the negative pressure gradient term approaching the trailing edge. Strong shear stress appears near the middle of the bearing and in the circumferential direction at locations with high dynamic viscosity caused by lower lubricant temperature at the oil supply inlets. This effect becomes stronger as rpm increases.

Figures 18(*c*) and 19(*c*) show shaft surface heat flux contours, where negative and positive values indicate cooling and heating of the shaft, respectively. It is seen that cooling of the shaft occurs mainly near the oil supply inlets. This BP cooling effect is not present in the Reynolds approach, which only includes pad domains and not supply oil inlets. The heat flux is seen to increase near the trailing edge of the pads.

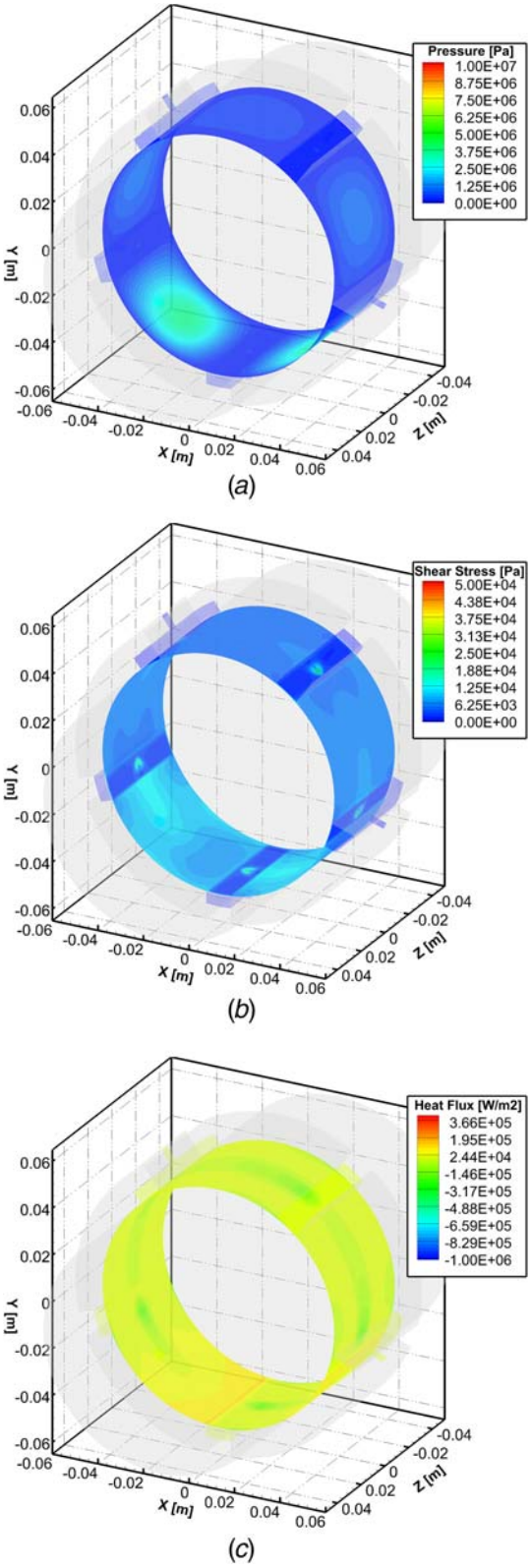

Fig. 18 CFD shaft surface contours "with mixing effect" condition at 3000 rpm: (*a*) pressure, (*b*) shear stress, and (*c*) heat flux

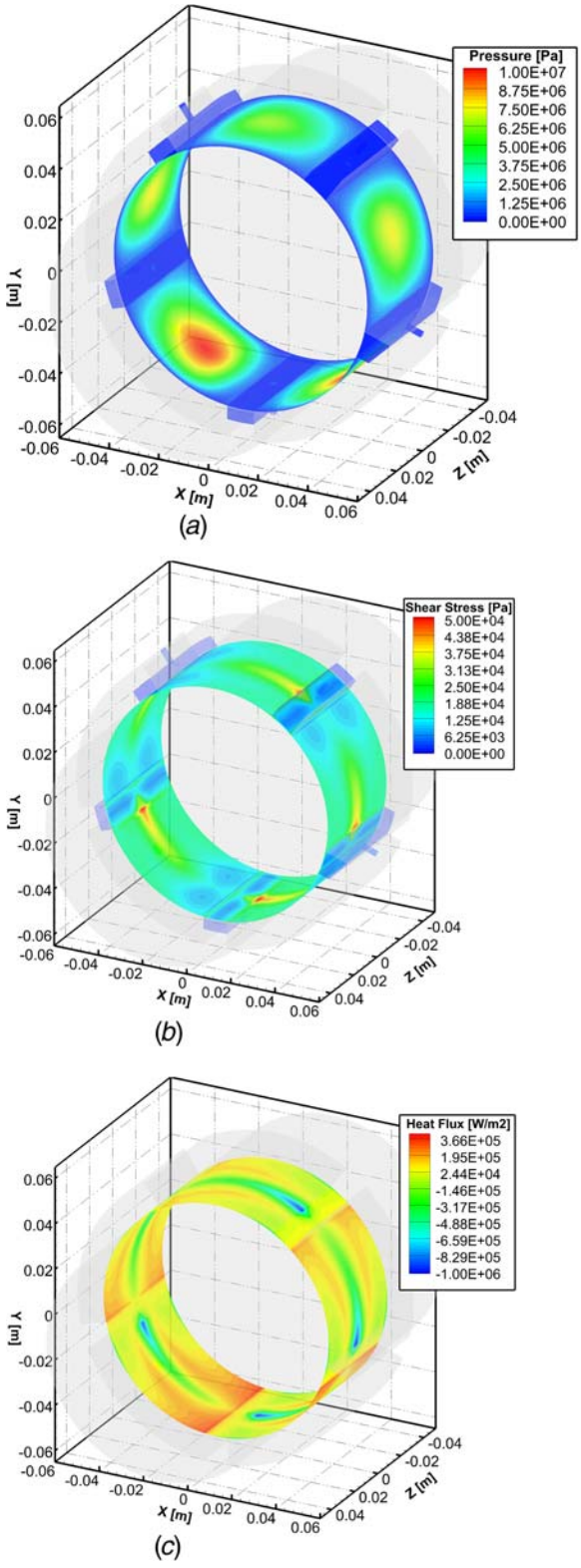

Fig. 19 CFD shaft surface contours "with mixing effect" condition at 15,000 rpm: (*a*) pressure, (*b*) shear stress, and (*c*) heat flux

The pressure, film thickness, heat flux, and temperature plots on the shaft surface are represented in Figs. 20–22. The results are obtained for the case C conditions. The distribution of the pressure along the bearing centerline is given in Fig. 20. The Reynolds model shows good agreement with the CFD model at a low operating speed, i.e., 3000 rpm (Fig. 20(*a*)), but a significant disparity occurs at a high operating speed, i.e., 15,000 rpm (Fig. 20(*b*)). This is consistent with Fig. 21(*b*), which shows that a thinner film thickness is predicted by the CFD model. Another characteristic in the CFD prediction is that there is a peak pressure between pads because of the sudden deceleration of the nozzle flow after entering the BP volume (Bernoulli Effect). When comparing the

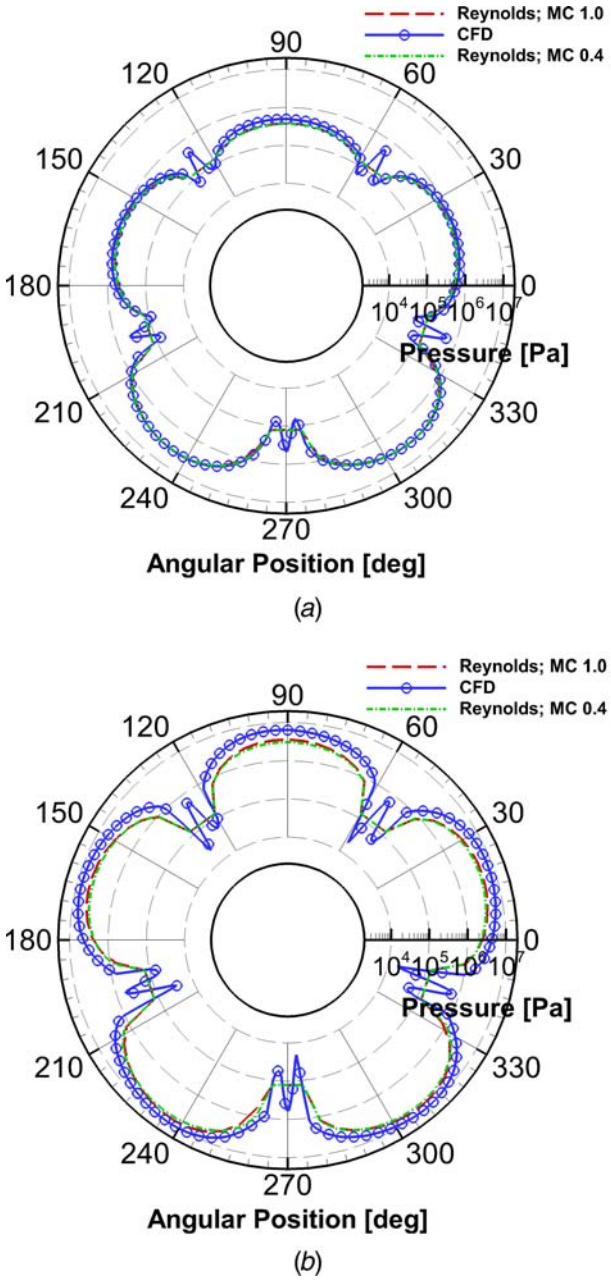

Fig. 20 Pressure distribution "with mixing effect" condition: (*a*) 3000 rpm and (*b*) 15,000 rpm

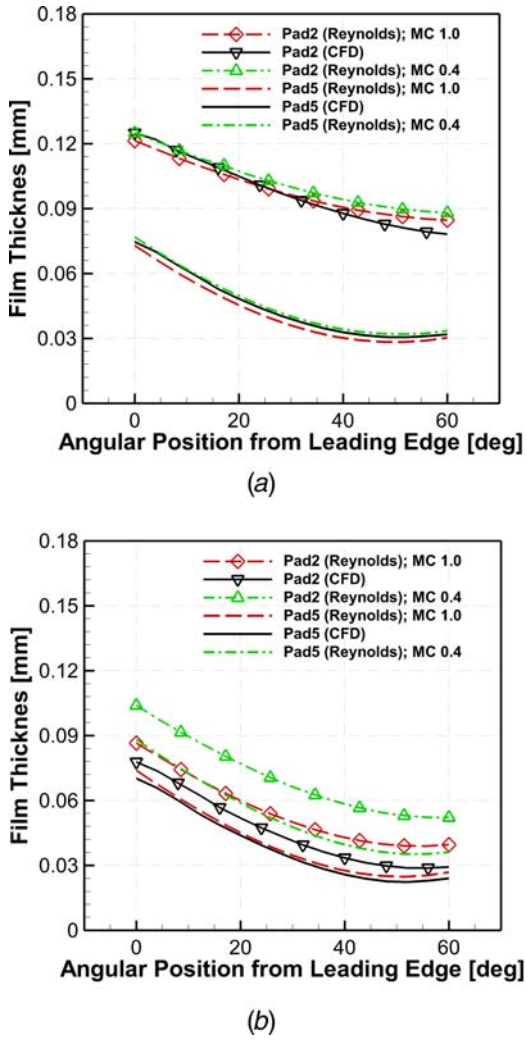

Fig. 21 Film Thickness "with mixing effect" condition: (*a*) 3000 rpm and (*b*) 15,000 rpm

Reynolds and CFD model, the film thickness is almost equal at a low speed, i.e., 3000 rpm, independent of MC value as presented in Fig. 21(*a*). However, a significant discrepancy occurs between the CFD and the Reynolds model at a high operating speed, i.e., 15,000 rpm, as shown in Fig. 21(*b*). This results from the difference of shaft thermal expansions in the two approaches. The results in Fig. 21 show that the CFD model predicts thinner film thickness.

Figure 22 clearly illustrates a primary cause for the disparity between the CFD and the Reynolds model. The CFD result in Fig. 22(*a*) shows that most of the cooling effect occurs near the oil inlets, and the shaft is heated near both sides of the bearing. The heating effect is more distinguishable at the trailing edge than at the leading edge because of the higher heat generation in the thinner film at the trailing edge. Figure 22(*b*) shows that the Reynolds and CFD have a large difference in heat flux prediction on the shaft surface. The CFD model predicts a significantly uneven heat flux distribution, which indicates uneven radial temperature profiles depending on the location, including the pad inlet. Figures 22(*c*) and 22(*d*) show a significant axial variation in the circumferential average temperature. This result implies that the MC should have an axial dependence; however, that dependence is unknown without the BP thermal flow CFD results or perhaps with strong intuitive skill based on the experience. These results show that the usual Reynolds modeling assumptions of uniform cross film (radial) temperature distribution and uniform MC in the axial direction at the pad inlets could yield large errors in the predicted temperatures. The CFD result indicates that the variation of the axial temperature distribution predicted at the pad inlet propagates in the circumferential direction and yields large differences between the Reynolds and CFD model over the entire domain of the lubricant film.

Figures 23 and 24 show surface temperature contours predicted by the CFD case C model for 3000 and 15,000 rpm operation, respectively. The overall temperature level is seen to increase with an increasing rpm, as expected from the higher viscous shearing—heat generation. The shaft temperature is almost uniform in the circumferential direction due to its high rotation rate and the much slower thermal time constants as mentioned. The axial temperature distribution is highly influenced by the oil injection effect. The pad temperature is seen to increase from leading to trailing edge, consistent with the heat flux plot in Figs. 19 and 22(*a*).

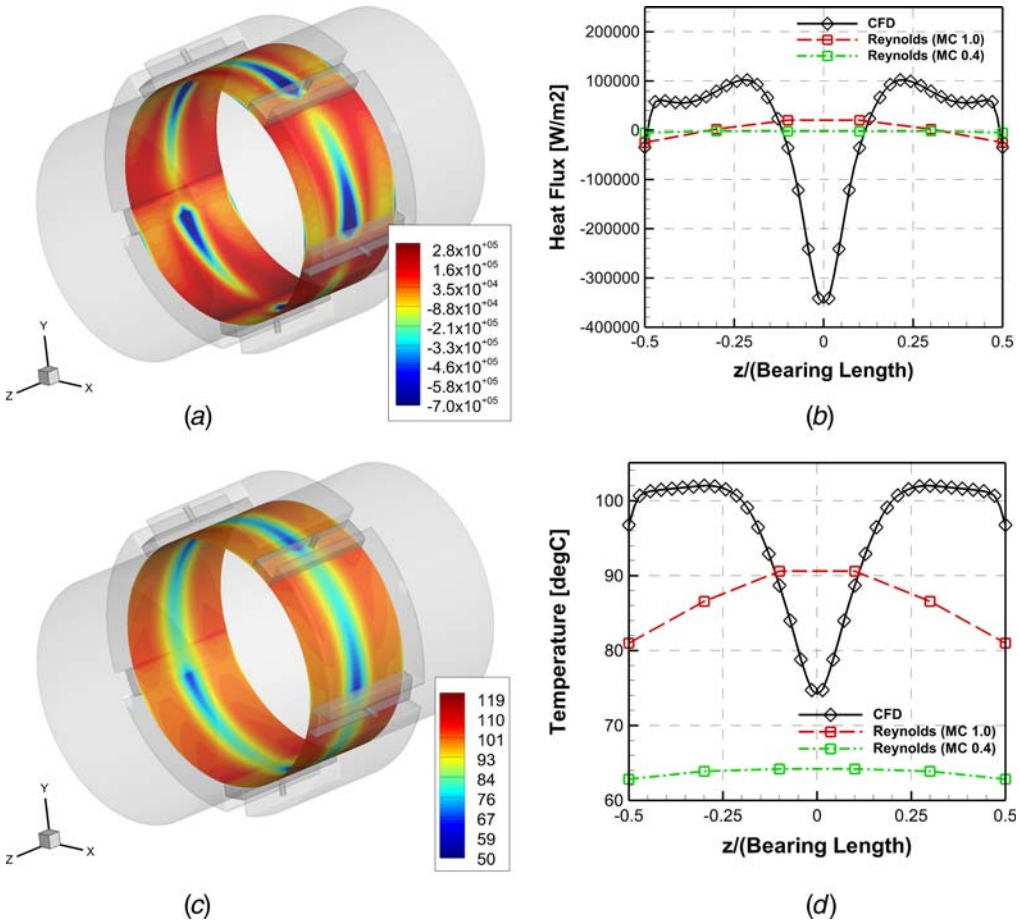

Fig. 22 Heat flux and temperature at shaft surface "with mixing effect": (*a*) heat flux (w/m^2), (*b*) circumferentially averaged heat flux distribution, (*c*) temperature (°C), and (*d*) circumferentially averaged temperature distribution

Turbulence occurs between pads due to the relatively large and discontinuous fluid flow passages, recirculation, and high Reynolds numbers. The gamma transitional model of turbulence enables modeling of simultaneously laminar and turbulent flows in different regions. Figure 25 shows turbulence occurring between pads 1 and 5 as indicated by the colored eddy viscosity contours. The eddy viscosity is almost 0 (laminar) close to the shaft, except for near the oil injection. This effect becomes more pronounced for the higher speed case. The velocity vectors in Fig. 25 reveal several large vortices generated in the BP region. These circulate and mix the lubricant, consistent with the basic assumption of the mixing theory.

5 Conclusion

Tilting pad journal bearing is ubiquitously utilized throughout the chemical process and in utility and defense industries and requires highly accurate response predictions to avoid premature wear and vibration related problems. This study presented a new three-dimensional CFD-based FSI modeling approach for a TPJB to improve the accuracy of the conventional Reynolds thin film approach. Part I focuses on static response prediction corresponding to the journal and pads being in nonvibrating states at the static equilibrium. Part II treats dynamic response characteristic prediction primarily directed toward accurate prediction of bearing stiffness and damping. To the best of the authors' knowledge, this is the first paper to utilize a full 3D RANS model for the TPJB simulation. The modeling approach presented has the following features for TPJB modeling: 3D multiphase flow, thermal-fluid, transitional turbulence, a thermal rotational shaft, pad tilting motion, nonlinear pivot flexibility, and deformation coupled with an FEA solver. A benefit of the CFD approach is the inherent high fidelity of modeling in the between pad BP regions where supply oil is mixed with carryover oil discharged from the pad trailing edges. This affects the pad leading edge temperature distributions, which in turn are shown to effect pad hot spot and shaft temperatures, along with operating eccentricity and attitude angle. This eliminates the guesswork of selecting a mixing coefficient, which is required in the Reynolds modeling approach, which as shown above can lead to significant errors in the response variable predictions. The TPJB CFD modeling approach presented earlier is presented with detailed instructions and algorithms for the treatment of boundary conditions, meshing techniques, iterative searches for equilibrium states, and so forth.

A detailed comparison between the new CFD approach and the conventional Reynolds approach was provided. The Reynolds approach was highly sophisticated including the capabilities of coupled thermal-elastic-hydrodynamic modeling, 3D energy equation and variable viscosity Reynolds equation solutions, cavitation, mixing theory, etc. The first comparison was for a pad-only model, neglecting the mixing occurring between pads. This was performed as an initial validation study for the CFD approach where a constant temperature distribution is applied to the film at the pad leading edges in both the Reynolds and the CFD models. The expectation and the outcome were that the two approaches should agree very closely because the inertia term, radial pressure distribution, and shaft curvature effect were neglected in the pad regions, and simplified pad inlet temperature distributions utilized in Reynolds TPJB models were also imposed on the CFD model.

The CFD results were then compared with the Reynolds model considering "with mixing effect," with the latter approach

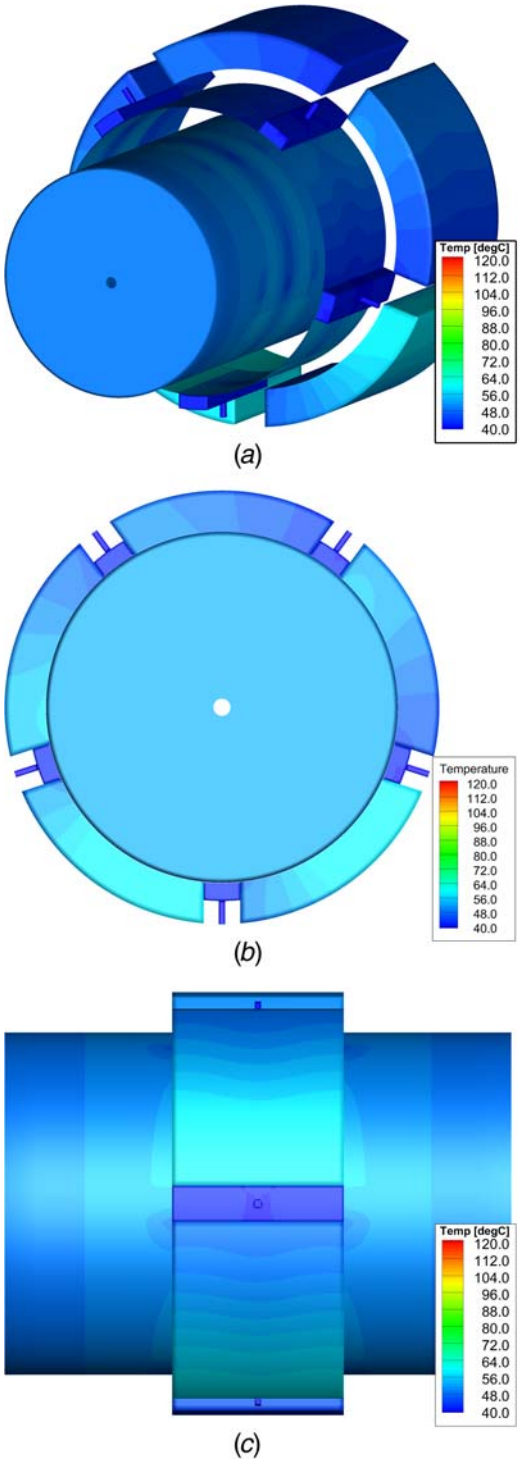

Fig. 23 Surface temperature contours "with mixing effect" at 3000 rpm: (*a*) overview, (*b*) *x–y* view, and (*c*) *x–z* view

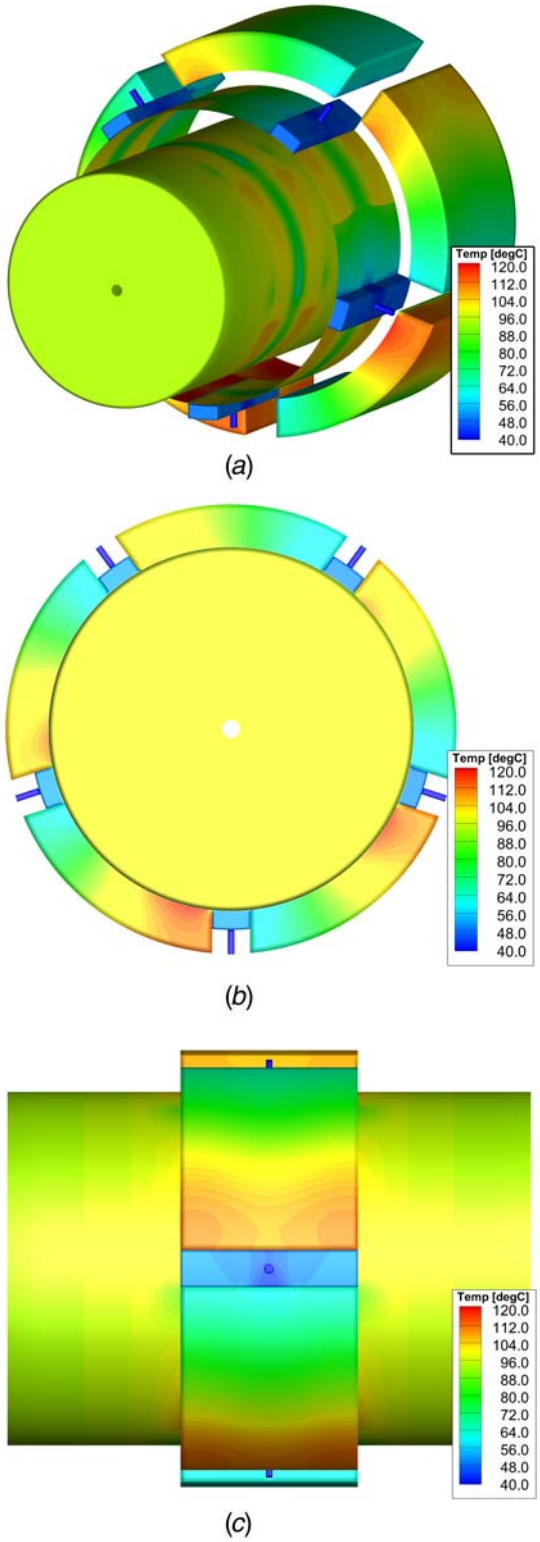

Fig. 24 Surface temperature contours "with mixing effect" condition at 15,000 rpm: (*a*) overview, (*b*) *x–y* view, and (*c*) *x–z* view

employing an MC to account for the mixing of fresh supply oil and pad carryover oil to obtain the temperature boundary conditions at the inlet to each pad. Inspection of the CFD model results revealed that the Reynolds model's neglect of the temperature distribution in the radial direction, and the nonuniform mixing effect in the axial direction at each pad's inlet, resulted in significant errors in most TPJB static response variables, compared with the high-fidelity CFD model results. The weakness of employing an MC in the Reynolds approach was highlighted with these errors, and also in the wide ranges of predictions for response variables depending on the choice of an MC value, which is presently done by rules of thumb and sparse empirical results.

The future work in the CFD TPJB modeling area will include seeking more computationally efficient hybridization of the two approaches to deliver high accuracy at the lower computational cost relative to a pure CFD approach. The present wall clock time required for a full static response simulation is 14.4 h when utilizing

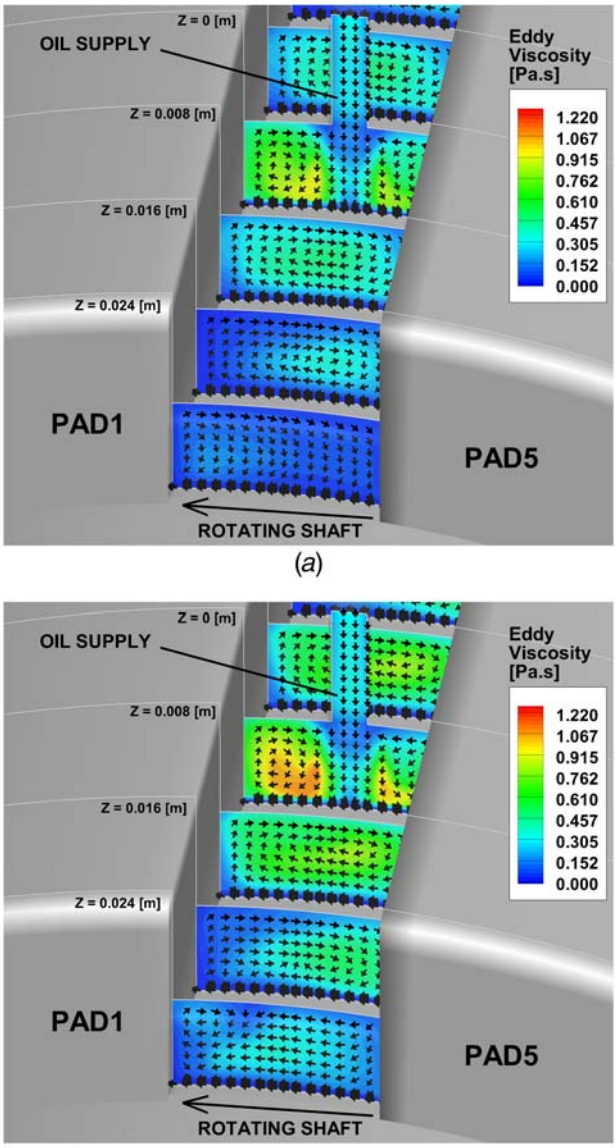

Fig. 25 Velocity vector field and eddy viscosity contour between pads 1 and 5: (*a*) 3000 rpm and (*b*) 15,000 rpm

12 cores of a computer server based on the dual Intel Xeon 2.5 GHz E5-2670 v2 10-core processors (TAMU High Performance Research Computing Center).

Acknowledgment

The authors gratefully acknowledge the funding received for this research from the Turbomachinery A&M Turbomachinery Research Consortium (TRC) and the Texas A&M High Performance Research Computing Center (HPRC).

Nomenclature

h = film thickness, m
k = turbulent kinetic energy, m^2/s^2
p = Pressure, Pa
r = volume faction
u = mean fluid velocity, m/s
A = Area, m^2
F = applied load, N
M = applied moment, Nm
R = Radius, m
T = Temperature, °C
$\dot{m}_\alpha$ = mass transfer rate into α phase by cavitation, kg/m^3
h_f = static enthalpy, J/kg
h_{tot} = mean total enthalpy, J/kg
u_s = shaft velocity, m/s
B_1 = blending function 1
C_F = empirical parameter
C_l = clearance, m
C_p = specific heat, J/kg K
C_R = relaxation factor
P_k = turbulence production due to viscous force W/m^3
S_M = momentum source per unit volume, N/m^3
S_E = energy source per unit volume, J/m^3s
γ = turbulence intermittency
Γ_{dis} = mesh stiffness
Δp_{pvt} = pad pivot displacement, m
Δx = x mesh displacement, m
Δy = y mesh displacement, m
Δx_s = shaft x mesh displacement, m
Δy_s = shaft y mesh displacement, m
$\Delta\delta_{tlt}$ = pad tilting angular displacement, deg
δ_i = mesh displacement, m
θ_p = center angle of pad, deg
λ = thermal conductivity, W/mK
μ = dynamic viscosity, $Pa \cdot s$
ρ = density, kg/m^3
τ = molecular stress tensor, N/m^2
ω = turbulent frequency, 1/s
Ω = rotating speed, 1/s
$[F]$ = load vector, N
$[K]$ = global stiffness matrix, N/m
$[u]$ = nodal displacement vector, m
$[\Delta X]$ = displacement vector, m
Pr = Prandtl number

Subscripts

0 = initial node position
b = bearing
bb = bubble
cav = cavitation
$cond$ = condensation
eff = effective
$evap$ = evaporation
f = fluid-film
l = liquid
nuc = nucleation site
p = pad
pvt = pivot motion
rct = reaction force generated by fluid-film
s = shaft
sup = supply
t = turbulent
TE = thermal expansion from FEA solver
te = thermal expansion applied to CFD solver
tlt = tilting motion
$trns$ = translational motion
tot = total
$trgt$ = target moment to equilibrium state
v = vapor phase
α = vapor or liquid phase

Superscripts

$cntr$ = centrifugal force
j = pad number
th = thermal
‘ = modified

Appendix

Derivation of total shaft and pad displacement vectors for equilibrium position search

$$[\Delta X_{p,tot}{}^{j}] = \begin{pmatrix} \Delta x_{p,tot}{}^{j} \\ \Delta y_{p,tot}{}^{j} \end{pmatrix} \tag{A1}$$

(Total displacement vector of nodes in jth pad)

$$[\Delta X_{s,tot}] = \begin{pmatrix} \Delta x_{s,tot} \\ \Delta y_{s,tot} \end{pmatrix} \tag{A2}$$

(Total displacement vector of nodes in shaft)

The relative change of the film thickness with respect to the previous nodal position is expressed in terms of the angular coordinate θ, utilizing the film thickness h^j corresponding to the jth pad given in Eq. (31)

$$\Delta h_p{}^{j}(\theta) = \Delta p_{pvt}{}^{j}\cos(\theta_p{}^{j})\cos(\theta) + \Delta p_{pvt}{}^{j}\sin(\theta_p{}^{j})\sin(\theta) - \Delta\delta_{tlt}{}^{j}R_s\sin(\theta - \theta_p{}^{j}) \tag{A3}$$

$$\Delta h_s(\theta) = -\Delta x_s\cos(\theta) - \Delta y_s\sin(\theta) \tag{A4}$$

During the iterative search for the equilibrium state the global coordinate x and y displacements of the pad and shaft surfaces, relative to previous nodal position, are updated. These increments are written in terms of variation of angular coordinate θ and the incremental film thicknesses as follows:

Pad tilting and pivot motion displacements as a function of (θ):

$$\Delta x_p{}^{j}(\theta) = \Delta h_p{}^{j}(\theta)\cos(\theta) \tag{A5}$$

$$\Delta y_p{}^{j}(\theta) = \Delta h_p{}^{j}(\theta)\sin(\theta) \tag{A6}$$

Shaft translational motion displacements as a function of (θ):

$$\Delta x_s(\theta) = \Delta h_s(\theta)\cos(\theta) \tag{A7}$$

$$\Delta y_s(\theta) = \Delta h_s(\theta)\sin(\theta) \tag{A8}$$

Substitution of (A3) and (A4) into (A5)—(A8) yields expressions for pad and shaft surface displacements relative to the previous nodal positions in terms of the pivot displacements($\Delta p_{pvt}{}^{j}$), journal displacements(Δx_s, Δy_s) and pad angles($\Delta\delta_{tlt}{}^{j}$) relative to the previous nodal position and the angular coordinate θ as pad tilting and pivot motion displacements as a function of (θ):

$$\Delta x_p{}^{j}(\theta) = \{\Delta p_{pvt}{}^{j}\cos(\theta_p{}^{j})\cos(\theta) + \Delta p_{pvt}{}^{j}\sin(\theta_p{}^{j})\sin(\theta) - \Delta\delta_{tlt}{}^{j}R_s\sin(\theta - \theta_p{}^{j})\}\cos(\theta) \tag{A9}$$

$$\Delta y_p{}^{j}(\theta) = \{\Delta p_{pvt}{}^{j}\cos(\theta_p{}^{j})\cos(\theta) + \Delta p_{pvt}{}^{j}\sin(\theta_p{}^{j})\sin(\theta) - \Delta\delta_{tlt}{}^{j}R_s\sin(\theta - \theta_p{}^{j})\}\sin(\theta) \tag{A10}$$

Shaft translational motion displacements as a function of (θ):

$$\Delta x_{s,trns}(\theta) = \{-\Delta x_s\cos(\theta) - \Delta y_s\sin(\theta)\}\cos(\theta) \tag{A11}$$

$$\Delta y_{s,trns}(\theta) = \{-\Delta x_s\cos(\theta) - \Delta y_s\sin(\theta)\}\sin(\theta) \tag{A12}$$

The initial x and y coordinate (x_0,y_0) of the nodes at shaft-film and pad–film interface boundaries are approximately

$$\cos(\theta) \simeq \frac{x_0}{R_s} \tag{A13}$$

$$\sin(\theta) \simeq \frac{y_0}{R_s} \tag{A14}$$

where the very thin film thickness between the shaft and pads has been neglected. Equations (A13) and (A14) are then substituted into (A9)—(A12) along with consideration of thermal expansions to obtain total displacements of the pad surface due to pad tilting, pivot displacements, and thermal displacements:

$$\Delta x_{p,tot}{}^{j}(x,y) = \left\{-\frac{\Delta\delta_{tlt}{}^{j}}{R_s}x_0(y_0\cos\theta_p{}^{j} - x_0\sin\theta_p{}^{j})\right\} + \left\{\frac{\Delta p_{pvt}{}^{j}}{R_s{}^{2}}x_0(x_0\cos\theta_p{}^{j} + y_0\sin\theta_p{}^{j})\right\} + \left\{-\frac{x_0}{R_s{}^{2}}(\Delta x_{p,TE}{}^{j}x_0 + \Delta y_{p,TE}{}^{j}y_0)\right\} \tag{A15}$$

$$\Delta y_{p,tot}{}^{j}(x,y) = \left\{-\frac{\Delta\delta_{tlt}{}^{j}}{R_s}y_0(y_0\cos\theta_p{}^{j} - x_0\sin\theta_p{}^{j})\right\} + \left\{\frac{\Delta p_{pvt}{}^{j}}{R_s{}^{2}}y_0(x_0\cos\theta_p{}^{j} + y_0\sin\theta_p{}^{j})\right\} + \left\{-\frac{y_0}{R_s{}^{2}}(\Delta x_{p,TE}{}^{j}x_0 + \Delta y_{p,TE}{}^{j}y_0)\right\} \tag{A16}$$

Total displacements of the journal surface due to shaft translation displacements and shaft thermal displacements:

$$\Delta x_{s,tot}(x,y) = \left\{\frac{x_0}{R_s{}^{2}}(\Delta x_s x_0 + \Delta y_s y_0)\right\} + \left\{\frac{x_0}{R_s{}^{2}}(\Delta x_{s,TE}x_0 + \Delta y_{s,TE}y_0)\right\} \tag{A17}$$

$$\Delta y_{s,tot}(x,y) = \left\{\frac{y_0}{R_s{}^{2}}(\Delta x_s x_0 + \Delta y_s y_0)\right\} + \left\{\frac{y_0}{R_s{}^{2}}(\Delta x_{s,TEe}x_0 + \Delta y_{s,TEe}y_0)\right\} \tag{A18}$$

References

[1] Tieu, A., 1973, "Oil-Film Temperature Distribution in an Infinitely Wide Slider Bearing: An Application of the Finite-Element Method," J. Mech. Eng. Sci., **15**(4), pp. 311–320.

[2] Ettles, C. M. M., 1980, "The Analysis and Performance of Pivoted Pad Journal Bearings Considering Thermal and Elastic Effects," ASME J. Lubr. Tech., **102**(2), pp. 182–191.

[3] Knight, J. D., and Barrett, L. E., 1987, "Analysis of Tilting-Pad Journal Bearing With Heat Transfer Effects," ASME J. Tribol., **110**(1), pp. 128–133.

[4] Brugier, D., and Pascal, M. T., 1989, "Influence of Elastic Deformations of Turbo-Generator Tilting Pad Bearings on the Static Behavior and on the Dynamic Coefficients in Different Designs," ASME J. Tribol., **111**(2), pp. 364–371.

[5] Taniguchi, S., Makino, T., Takeshita, K., and Ichimura, T., 1990, "A Thermohydrodynamic Analysis of Large Tilting-Pad Journal Bearing in Laminar and Turbulent Flow Regimes With Mixing," ASME J. Tribol., **112**(3), pp. 542–550.

[6] Kim, J., Palazzolo, A. B., and Gadangi, R. K., 1994, "TEHD Analysis for Tilting-Pad Journal Bearings Using Upwind Finite Element Method," Tribo. Trans., **37**(4), pp. 771–783.

[7] Haugaard, A. M., and Santos, I. F., 2010, "Multi-Orifice Active Tilting-Pad Journal Bearings-Harnessing of Synergetic Coupling Effects," Tribol. Int., **43**(8), pp. 1374–1391.

[8] Suh, J., and Palazzolo, A. B., 2015, "Three-Dimensional Dynamic Model of TEHD Tilting-Pad Journal Bearing-Part I: Theoretical Modeling," ASME J. Tribol., **137**(4), p. 041704.

[9] Tong, X., Palazzolo, A. B., and Suh, J., 2016, "Rotodynamic Morton Effect Simulation With Transient, Thermal Shaft Bow," ASME J. Tribol., **138**, p. 031705.

[10] Dang, P. V., Chatterton, S., Pennacchi, P., and Vania, A., 2016, "Effect of the Load Direction on Non-Nominal Five-Pad Tilting-Pad Journal Bearings," Tribol. Int., **98**, pp. 197–211.

[11] Dang, P. V., Chatterton, S., Pennacchi, P., and Vania, A., 2016, "Numerical Investigation of the Effect of Manufacturing Errors in Pads on the Behavior of Tilting-Pad Journal Bearings," Proc. IME J. J. Eng. Tribol., **232**(4), pp. 480–500.

[12] Ettles, C., 1967, "Solutions for Flow in a Bearing Groove," Proc. Instn. Mech. Eng., **182**(14), pp. 120–131.

[13] Ettles, C., 1969, "Hot Oil Carry-Over in Thrust Bearings," Proc. Instn. Mech. Eng., **184**(12), pp. 75–81.

[14] Mitsui, J., Hori, H., and Tanaka, M., 1983, "Thermohydrodynamic Analysis of Cooling Effect of Supply Oil in Circular Journal Bearing," ASME J. Lubr. Tech., **105**(3), pp. 414–420.
[15] Heshmat, H., and Pinkus, O., 1986, "Mixing Inlet Temperature in Hydrodynamic Bearing," ASME J. Tribol., **108**(2), pp. 231–248.
[16] Boncompain, R., Fillon, M., and Frene, J., 1986, "Analysis of Thermal Effects in Hydrodynamic Bearings," ASME J. Tribol., **108**(2), pp. 219–224.
[17] Lin, Q., Wei, Z., Wang, N., and Chen, W., 2013, "Analysis on the Lubrication Performances of Journal Bearing System Using Computational Fluid Dynamics and Fluid-Structure Interaction Considering Thermal Influence and Cavitation," Tribol. Int., **64**, pp. 8–15.
[18] Chen, P. Y. P., and Hahn, E. J., 1998, "Use of Computational Fluid Dynamics in Hydrodynamic Lubrication," Proc. IME J. J. Eng. Tribol., **212**(6), pp. 427–436.
[19] Guo, Z., Toshio, H., and Gorden, R., 2005, "Application of CFD Analysis for Rotating Machinery: Part 1—Hydrodynamic, Hydrostatic Bearings and Squeeze Film Damper," ASME J. Eng. Gas Turbines Power, **4**, pp. 445–451.
[20] Shenoy, B. S., Pai, R. S., Rao, D. S., and Pai, R., 2009, "Elasto-Hydrodynamic Lubrication Analysis of Full 360° Journal Bearing Using CFD and FSI Techniques," World J. Model Simulat., **5**(4), pp. 315–320.
[21] Liu, H., Xu, H., Ellison, P. J., and Jin, Z., 2010, "Application of Computational Fluid Dynamics and Fluid-Structure Interaction Method to the Lubrication Study of a Rotor-Bearing System," Tribol. Lett., **38**, pp. 324–336.
[22] Edney, L. E., Heitland, G. B., and Decalmillo, S. M. (1998). "Testing, Analysis, and CFD Modeling of a Profiled Leading Edge Groove Tilting Pad Journal Bearing," 1998 ASME TURBO EXPO Conference, Stockholm, Sweden, June 2–5, ASME Paper No. 98-GT-409.
[23] Armentrout, R. W., He, M., Haykin, T., and Reed, A. E., 2017, "Analysis of Turbulence and Convective Inertia in a Water-Lubricated Tilting-Pad Journal Bearing Using Conventional and CFD Approaches," Tribol. Trans., **60**(6), pp. 1129–1147.
[24] Menter, F. R., Smirnov, P. E., Liu, T., and Avancha, F. R. (2015). "A One-Equation Local Correlation-Based Transition Model," Flow, Turbul. Combust., **95**(4), pp. 583–619.
[25] Gadangi, R., and Palazzolo, A., 1995, "Transient Analysis of Tilt Pad Journal Bearings Including Effects of Pad Flexibility and Fluid Film Temperature," ASME J. Tribol., **117**(3), pp. 123–135.
[26] Kirk, R., and Reedy, S., 1988, "Evaluation of Pivot Stiffness for Typical Tilting-Pad Journal Bearing Designs," ASME J. Vib. Acoust. Stress Reliab. Des., **110**(2), pp. 165–171.
[27] Young, W. C., and Budynas, R. G., 2002, *Roak's Formulas for Stress and Strain*, McGraw-Hill, New York.
[28] Nicholas, J. C., and Wygant, K. (1995). "Tilting Pad Journal Bearing Pivot Design for High Load Applications," Proceedings of the 24th Turbomachinery Symposium, Texas A&M University, College Station, TX, pp. 33–47.